Internal-tide interactions with the Gulf Stream and Middle Atlantic Bight shelfbreak front

Massachusetts Institute of Technology

RESEARCH ARTICLE

Key Points:
- Simulations of the MAB reveal internal-tide interactions with the Gulf Stream and shelfbreak front
- The shelfbreak front decreases topographic generation and alters the arrival times of internal tides
- Tide-mean-flow interactions in the Gulf Stream are explained by terms in the mode-1 momentum/energy balance

Correspondence to:
S. M. Kelly,
smkelly@d.umn.edu

Internal-tide interactions with the Gulf Stream and Middle Atlantic Bight shelfbreak front

Samuel M. Kelly[1,2] and Pierre F. J. Lermusiaux[2]

[1]Large Lakes Observatory and Department of Physics, University of Minneosta Duluth, Duluth, Minnesota, USA,
[2]Department of Mechanical Engineering, Massachusetts Institute of Technology, Cambridge, Massachusetts, USA

Abstract Internal tides in the Middle Atlantic Bight region are found to be noticeably influenced by the presence of the shelfbreak front and the Gulf Stream, using a combination of observations, equations, and data-driven model simulations. To identify the dominant interactions of these waves with subtidal flows, vertical-mode momentum and energy partial differential equations are derived for small-amplitude waves in a horizontally and vertically sheared mean flow and in a horizontally and vertically variable density field. First, the energy balances are examined in idealized simulations with mode-1 internal tides propagating across and along the Gulf Stream. Next, the fully nonlinear dynamics of regional tide-mean-flow interactions are simulated with a primitive-equation model, which incorporates realistic summer-mesoscale features and atmospheric forcing. The shelfbreak front, which has horizontally variable stratification, decreases topographic internal-tide generation by about 10% and alters the wavelengths and arrival times of locally generated mode-1 internal tides on the shelf and in the abyss. The (sub)mesoscale variability at the front and on the shelf, as well as the summer stratification itself, also alter internal-tide propagation. The Gulf Stream produces anomalous regions of $\mathcal{O}(20 \text{ mW m}^{-2})$ mode-1 internal-tide energy-flux divergence, which are explained by tide-mean-flow terms in the mode-1 energy balance. Advection explains most tide-mean-flow interaction, suggesting that geometric wave theory explains mode-1 reflection and refraction at the Gulf Stream. Geometric theory predicts that offshore-propagating mode-1 internal tides that strike the Gulf Stream at oblique angles (more than thirty degrees from normal) are reflected back to the coastal ocean, preventing their radiation into the central North Atlantic.

1. Introduction

Internal tides (baroclinic tides) are generated where surface tides (barotropic tides) heave stratified water vertically at sloped topography [e.g., continental slopes and mid-ocean ridges; *Garrett and Kunze*, 2007]. Globally, this process drains surface tides of their energy; internal tides are generated at a rate of about 1 TW [*Egbert and Ray*, 2003] and additional energy is lost through turbulent dissipation. Most deep-ocean internal-tide energy is contained within low vertical modes [e.g., *Hendry*, 1977; *Nash et al.*, 2006; *Alford et al.*, 2007], which typically propagate as linear waves because their particle speeds are smaller than their wave speeds [e.g., *St. Laurent and Garrett*, 2002; *Klymak et al.*, 2013]. However, internal-tide generation [e.g., *Chuang and Wang*, 1981] and propagation [e.g., *Park and Watts*, 2006; *Rainville and Pinkel*, 2006; *Zaron and Egbert*, 2014] can be significantly altered by interactions with slowly varying (or steady) mean-flow currents and with a horizontally variable density field. Therefore, accurate predictions of internal tides in regions with strong subtidal flows, such as the coastal ocean, require proper handling of these interactions. Improved internal-tide predictions in the coastal ocean can increase our understanding of nonlinear internal-wave generation [*Nash et al.*, 2012], ecological productivity [*Sharples et al.*, 2009], and sound propagation [*Tang et al.*, 2007; *Lermusiaux et al.*, 2010; *Duda et al.*, 2014a].

Here we examine internal-tide dynamics in the Middle Atlantic Bight region during the 2006 Shallow Water and Autonomous Wide Aperture Cluster for Surveillance experiments (SW06) [*Tang et al.*, 2007; *Newhall et al.*, 2007; *Chapman and Lynch*, 2010]. During July to September 2006, a large set of oceanographic and acoustic measurements were collected in the Middle Atlantic Bight region. Ocean primitive-equation forecasts with data assimilation, reanalyses, and adaptive sampling recommendations were also issued in real-time in support of the experiment [*Lermusiaux et al.*, 2006; *Haley and Lermusiaux*, 2010; *Lin et al.*, 2010].
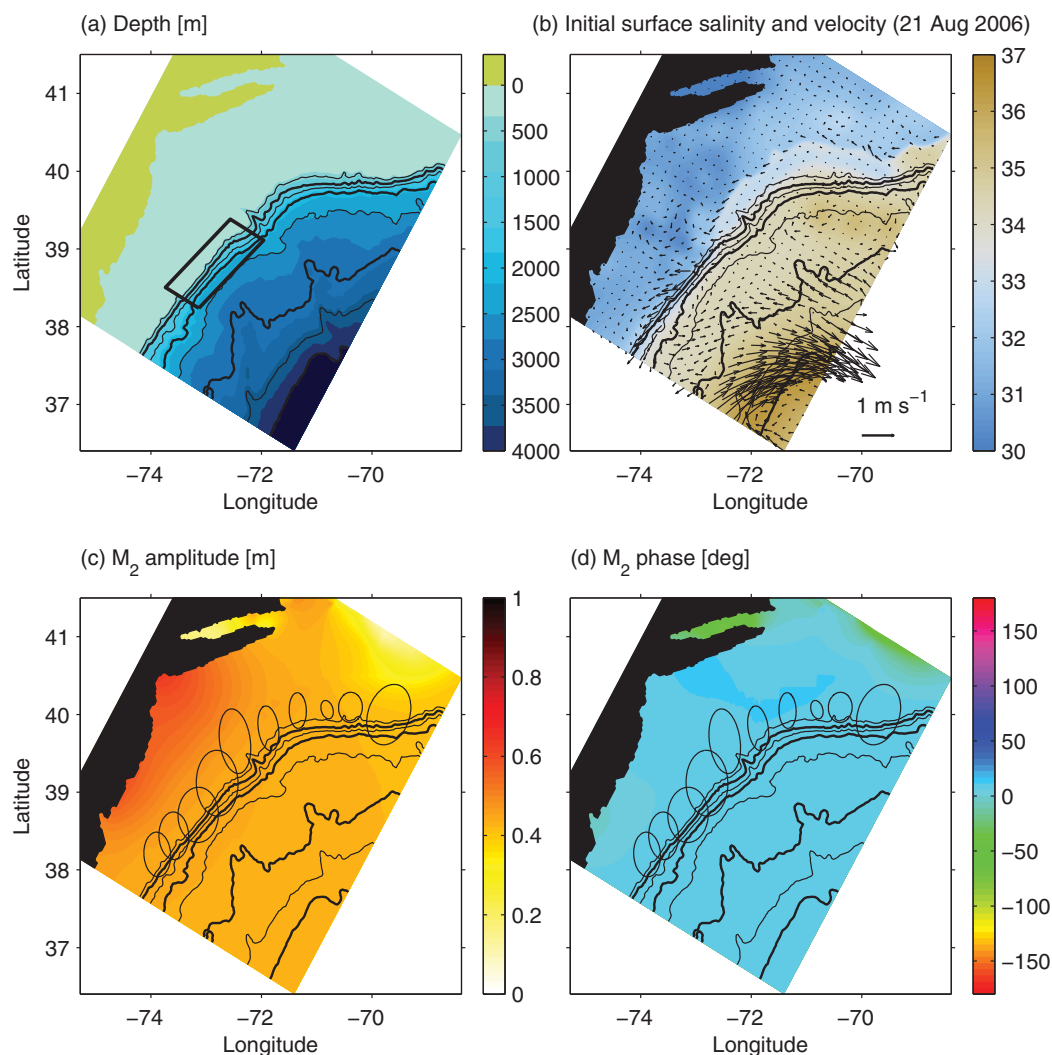
Figure 1. (a) The MSEAS data-driven primitive-equation simulations for the 2006 summer conditions include realistic topography and (b) salinity fronts due to the shelfbreak and Gulf Stream. (c) The surface tide is approximately 0.5 m, (d) has nearly uniform phase, and contains a significant cross-slope component (excursion ellipses ×30). The box indicates the main site of the SW06 experiment. The MSEAS grid is rotated, following the coastline, with horizontal velocities and gradients defined along this grid.

Further studies of ocean reanalyses called attention to interactions of large-scale internal tides with two energetic and persistent mean flows: the summer shelfbreak front and the Gulf Stream (Figure 1). The purpose of this paper is to (i) describe the magnitude and character of the effects of these flows and their density fields on the stationary (i.e., coherent) internal tide and (ii) identify the dominant momentum and energy pathways of the tide-mean-flow interactions.

Numerous studies of internal tides and waves at the continental margins have emphasized simplified geometries and/or cross-slope dynamics, with well established results, e.g., see the reviews of theoretical, numerical, and laboratory studies by *Huthnance* [1995], *Holloway et al.* [2002], *Helfrich and Melville* [2006], *Klymak et al.* [2011], *Ivey* [2011], *Lamb* [2014], and references therein. However, only a few studies have examined tide-shelfbreak-front interactions under realistic conditions with complex geometries. One study of tide-shelfbreak-front dynamics is the linearized two-dimensional modeling study of *Chuang and Wang* [1981], which concluded that internal-tide generation is suppressed where the topography and shelfbreak-front isopycnals slope in the same direction. *Chen et al.* [2003] examined the influence of a shelfbreak front on internal-tide generation using idealized two-dimensional numerical simulations, but this work does not match well with SW06 conditions, in part because the authors did not include vertical stratification on the shelf. Here we utilize fully nonlinear three-dimensional primitive-equation simulations, which incorporate

realistic topography and an observation-based shelfbreak front. This allows us to reassess these previous results in regard to summer conditions in the Middle Atlantic Bight region. Examining momentum and energy balances, we identify internal-tide interactions with the mean-flow current and density fields in the region.

Theoretical studies indicate that mean flows can refract low-mode internal tides [e.g., *Rainville and Pinkel*, 2006]. Observations [*Rainville and Pinkel*, 2004] and numerical models [*Pereira et al.*, 2007] even suggest that refraction by western-boundary currents, such as the Kuroshio and Brazil current, respectively, may be strong enough to reflect internal-tides that are generated at the coast as they propagate offshore, effectively blocking their radiation into the open ocean. In addition, *Kunze* [1985] used ray tracing to show that geostrophic vorticity can increase the frequency of the low-frequency bound of the internal-wave continuum, creating a barrier to internal-wave propagation that is analogous to a turning latitude. Here we assess low-mode internal-tide refraction and reflection in the Gulf Stream, starting again from primitive-equation momentum and energy conservation, and keeping the relevant interaction terms.

In the following analysis, we use realistic data-driven numerical simulations to quantify the momentum and energy pathways of internal-tide interactions with the shelfbreak front and the Gulf Stream. In section 2, we derive modal momentum and energy balances for small-amplitude internal tides in the presence of vertically and horizontally sheared mean-flow currents and a vertically and horizontally variable mean-density field. Section 3 describes our methods of simulating and analyzing internal tides. Section 4 analyzes idealized simulations of tide-mesoscale interactions. Section 5 analyzes the general effects of mesoscale circulation on internal tides in the Middle Atlantic Bight region. Sections 6 and 7 describe specific aspects of internal-tide interactions with the shelfbreak front and Gulf Stream, respectively. Section 8 presents our conclusions.

2. Theory

Most previous studies of internal tide-mesoscale interactions have used two-dimensional or three-dimensional ray tracing. *Rainville and Pinkel* [2006] decomposed tides into independent vertical modes and tracked their propagation using horizontal ray tracing. Their method is attractive because most internal-tide energy flux is carried by the lowest few modes. However, *Chavanne et al.* [2010] reverted to full three-dimensional ray tracing, because *Rainville and Pinkel*'s [2006] model did not incorporate modal coupling due to vertically sheared mean flows and sloping topography. Here we combine these approaches, and also build upon the analyses of *Zaron and Egbert* [2014]. We derive momentum and energy balances for small-amplitude waves in subtidal (or steady) spatially variable shear flow and density fields, keeping the corresponding nonlinear interaction terms. The resulting equations describe the horizontal propagation of individual tidal modes through spatially variable background/mean fields, incorporating the effects of vertical variability through intermodal coupling.

The inviscid hydrostatic nonlinear momentum, buoyancy (internal energy with a linearized equation of state), and continuity equations are:

$$\frac{D\mathbf{u}_{tot}}{Dt} + \mathbf{f} \times \mathbf{u}_{tot} = -\nabla p_{tot}, \tag{1a}$$

$$0 = -\frac{\partial p_{tot}}{\partial z} + b_{tot}, \tag{1b}$$

$$\frac{Db_{tot}}{Dt} = 0, \tag{1c}$$

$$\nabla \cdot \mathbf{u}_{tot} + \frac{\partial w_{tot}}{\partial z} = 0, \tag{1d}$$

respectively, where D/Dt is the total material derivative, ∇ the horizontal gradient, $\mathbf{u}_{tot}$ the horizontal velocity, w_{tot} the vertical velocity, $b = -g(\rho - \rho_0)/\rho_0$ the buoyancy perturbation scaled by ρ_0, ρ the density, ρ_0 the reference density, and p_{tot} the reduced pressure (pressure divided by density). The surface and bottom are located at $z = 0$ and $z = -H$, respectively. Next, we first assume a flat bottom and employ a rigid-lid approximation to simplify the derivations, but the effects of a sloping bottom are discussed and added in section 2.3.

2.1. Hydrostatic Tidal Waves Interacting With a Background Ocean

Consider a tidal wave with single frequency ω superimposed on a sufficiently slowly varying (or steady) mean flow and buoyancy fields,

$$\mathbf{u}_{tot} \approx \mathbf{u}(\mathbf{x},z,t) + \overline{\mathbf{U}}(\mathbf{x},z,t), \tag{2a}$$

$$w_{tot} \approx w(\mathbf{x},z,t) + \bar{W}(\mathbf{x},z,t), \tag{2b}$$

$$p_{tot} \approx p(\mathbf{x},z,t) + \bar{P}(\mathbf{x},z,t), \tag{2c}$$

$$b_{tot} \approx b(\mathbf{x},z,t) + \bar{B}(\mathbf{x},z,t), \tag{2d}$$

where lower-case letters are monochromatic wave components and upper-case letters with overbars are the slowly varying fields (background/mean currents, pressure, and buoyancy).

Substituting (2) into (1), we first average the inviscid primitive equations (1a) over sufficient tidal periods such that all terms linear in the monochromatic wave components average out, e.g., $\overline{\mathbf{u}_{tot}} = \overline{\mathbf{U}}$, etc. The result is the slowly varying nonlinear mean-flow and buoyancy equations (a more formal analysis consists of a two time scales decomposition for the mean and wave scales),

$$\frac{\partial \overline{\mathbf{U}}}{\partial t} + (\overline{\mathbf{U}} \cdot \nabla)\overline{\mathbf{U}} + \overline{(\mathbf{u} \cdot \nabla)\mathbf{u}} + \bar{W}\frac{\partial \overline{\mathbf{U}}}{\partial z} + \overline{w\frac{\partial \mathbf{u}}{\partial z}} + \mathbf{f} \times \overline{\mathbf{U}} = -\nabla\bar{P}, \tag{3a}$$

$$0 = -\frac{\partial \bar{P}}{\partial z} + \bar{B}, \tag{3b}$$

$$\frac{\partial \bar{B}}{\partial t} + \overline{\mathbf{U}} \cdot \nabla\bar{B} + \overline{\mathbf{u} \cdot \nabla b} + \bar{W}\frac{\partial \bar{B}}{\partial z} + \overline{w\frac{\partial b}{\partial z}} = 0, \tag{3c}$$

$$\nabla \cdot \overline{\mathbf{U}} + \frac{\partial \bar{W}}{\partial z} = 0. \tag{3d}$$

We then subtract the slowly varying fields equations (3a) from the primitive equations (1a) to obtain the tidal wave equations,

$$\frac{\partial \mathbf{u}}{\partial t} + (\overline{\mathbf{U}} \cdot \nabla)\mathbf{u} + (\mathbf{u} \cdot \nabla)\overline{\mathbf{U}} + (\mathbf{u} \cdot \nabla)\mathbf{u} - \overline{(\mathbf{u} \cdot \nabla)\mathbf{u}} + \bar{W}\frac{\partial \mathbf{u}}{\partial z} + w\frac{\partial \overline{\mathbf{U}}}{\partial z} + w\frac{\partial \mathbf{u}}{\partial z} - \overline{w\frac{\partial \mathbf{u}}{\partial z}} + \mathbf{f} \times \mathbf{u} = -\nabla p, \tag{4a}$$

$$0 = -\frac{\partial p}{\partial z} + b, \tag{4b}$$

$$\frac{\partial b}{\partial t} + \overline{\mathbf{U}} \cdot \nabla b + \mathbf{u} \cdot \nabla\bar{B} + \mathbf{u} \cdot \nabla b - \overline{\mathbf{u} \cdot \nabla b} + \bar{W}\frac{\partial b}{\partial z} + w\frac{\partial \bar{B}}{\partial z} + w\frac{\partial b}{\partial z} - \overline{w\frac{\partial b}{\partial z}} = 0, \tag{4c}$$

$$\nabla \cdot \mathbf{u} + \frac{\partial w}{\partial z} = 0. \tag{4d}$$

We next assume that wave amplitudes are small enough such that we can drop the wave-wave advection terms when compared to the other terms. This produces the following system of equations describing small-amplitude hydrostatic waves that nonlinearly interact with the background ocean,

$$\frac{\partial \mathbf{u}}{\partial t} + (\overline{\mathbf{U}} \cdot \nabla)\mathbf{u} + (\mathbf{u} \cdot \nabla)\overline{\mathbf{U}} + \bar{W}\frac{\partial \mathbf{u}}{\partial z} + w\frac{\partial \overline{\mathbf{U}}}{\partial z} + \mathbf{f} \times \mathbf{u} = -\nabla p, \tag{5a}$$

$$0 = -\frac{\partial p}{\partial z} + b, \tag{5b}$$

$$\frac{\partial b}{\partial t} + \overline{\mathbf{U}} \cdot \nabla b + \mathbf{u} \cdot \nabla\bar{B} + \bar{W}\frac{\partial b}{\partial z} + wN^2 = 0, \tag{5c}$$

$$\nabla \cdot \mathbf{u} + \frac{\partial w}{\partial z} = 0, \tag{5d}$$

where $N^2(\mathbf{x},z,t) \equiv \partial \bar{B}/\partial z$ is the slowly varying buoyancy frequency squared. The wave-mean advection terms in (5a) and (5c) are the sources of nonlinear interactions between waves and the slowly varying,

spatially variable, mean flow and buoyancy fields [see e.g., *Kunze*, 1985]. They are often neglected but will play a critical role in our analysis.

The tidally averaged depth-integrated total (barotropic and baroclinic) tidal-energy equation is now obtained. First, we take the dot product of (5a)–(5b) with velocity (**u**,*w*) and use (5d). The buoyancy work quantity *wb* in the vertical momentum equation (5b) is then eliminated by substituting the product of (5c) with b/N^2 (leading to the potential energy terms). Finally, the resulting energy equation is averaged over a tidal period and depth integrated, again for now assuming a flat bottom and rigid lid. The result is,

$$\nabla \cdot \langle \mathbf{F} \rangle + \langle A \rangle = \langle P^S \rangle + \langle P^B \rangle, \tag{6}$$

where $\langle \cdot \rangle$ denotes the average over a wave period. In (6), the energy tendency is null because the waves are assumed to be perfectly harmonic. The remaining terms are the averages of the energy flux (**F**), wave energy advection by the mean flow (*A*), shear production (P^S), and horizontal buoyancy production (P^B), which are, respectively:

$$\mathbf{F} = \int_{-H}^{0} \mathbf{u}p \, dz, \tag{7a}$$

$$A = \int_{-H}^{0} \left[\overline{\mathbf{U}} \cdot \nabla \left(\frac{\mathbf{u} \cdot \mathbf{u}}{2} \right) + \frac{\overline{\mathbf{U}}}{N^2} \cdot \nabla \left(\frac{b^2}{2} \right) + \bar{W} \frac{\partial}{\partial z} \left(\frac{\mathbf{u} \cdot \mathbf{u}}{2} \right) + \frac{\bar{W}}{N^2} \frac{\partial}{\partial z} \left(\frac{b^2}{2} \right) \right] dz, \tag{7b}$$

$$P^S = -\int_{-H}^{0} \left[\mathbf{u} \cdot (\mathbf{u} \cdot \nabla) \overline{\mathbf{U}} + w\mathbf{u} \cdot \frac{\partial \overline{\mathbf{U}}}{\partial z} \right] dz, \tag{7c}$$

$$P^B = -\int_{-H}^{0} \frac{b}{N^2} \mathbf{u} \cdot \nabla \bar{B} \, dz. \tag{7d}$$

Note that we can approximate *A* as $\int_{-H}^{0} \left[\overline{\mathbf{U}} \cdot \nabla \left(\frac{\mathbf{u} \cdot \mathbf{u}}{2} + \frac{b^2}{2N^2} \right) + \bar{W} \frac{\partial}{\partial z} \left(\frac{\mathbf{u} \cdot \mathbf{u}}{2} + \frac{b^2}{2N^2} \right) \right] dz$ if we neglect terms involving second derivatives of $\bar{B}$ (i.e., ∇N^{-2} and $\frac{\partial N^{-2}}{\partial z}$). The advection term quantifies the transport of tidal energy by the mean flow, but does not convert mean-flow energy to tidal energy. The shear-production and buoyancy-production terms quantify energy conversion between the mean flow and the tide, and appear with opposite signs in the mean-flow energy equations (not shown). They show that energy conversion only occurs where the mean flow has horizontal or vertical shear, or the background-density field has a horizontal shear. P^S and P^B are analogous to the production terms appearing in the turbulent-kinetic-energy equation [e.g., *Tennekes and Lumley*, 1972], although the balance here accounts for total (kinetic plus potential) wave energy and the "fluctuation" terms here are coherent monochromatic wave components with governing equations (5).

2.2. Projection onto *Vertical Modes*

The tidal-energy balance above is useful for quantifying net tide-mean-flow interactions, but does not provide information about the energy and momentum balances of individual vertical modes. Analyzing tides in terms of local vertical modes is convenient because the modes form a complete local orthogonal basis that separates barotropic motions and efficiently captures the vertical variability of the baroclinic motions. Hence, we consider local vertical modes and define the associated decomposition of velocity and pressure fields,

$$w(\mathbf{x}, z, t) = \sum_{n=0}^{\infty} w_n(\mathbf{x}, t) \Phi_n(\mathbf{x}, z), \tag{8a}$$

$$[\mathbf{u}(\mathbf{x}, z, t), p(\mathbf{x}, z, t)] = \sum_{n=0}^{\infty} [\mathbf{u}_n(\mathbf{x}, t), p_n(\mathbf{x}, t)] \phi_n(\mathbf{x}, z), \tag{8b}$$

where *n* is the mode number and $\phi_n = \partial \Phi_n / \partial z$. Note that if ϕ_n is defined to be unitless, then Φ_n has units of m. Therefore, u_n and p_n have conventional units, while w_n has units s^{-1} instead of m s^{-1}. The vertical modes are local: they are determined for each horizontal location by solving the hydrostatic eigenvalue problem:

$$\frac{\partial^2 \Phi_n}{\partial z^2} + \frac{N^2}{c_n^2} \Phi_n = 0 , \tag{9}$$

where c_n are eigenspeeds. The modes obey rigid-lid and flat bottom conditions, which require $\Phi_n = 0$ at the upper and lower boundaries. The eigenfunctions are normalized to obey the local orthogonality conditions:

$$\int_{-H}^{0} \Phi_m \Phi_n N^2 \, dz = c_n^2 H \delta_{mn}, \tag{10a}$$

$$\int_{-H}^{0} \phi_m \phi_n \, dz = H \delta_{mn} . \tag{10b}$$

Note that because Φ_n are orthogonal with weighting function $N^2(z)$, the normalization factor c_n^2 is only relevant when $m = n$; i.e., it is equivalent to $c_m c_n$ or c_m^2.

In what follows, we will assume that the terms involving mean-flow vertical velocities $\bar{W}$ can be neglected. This is appropriate in many situations, but if it is not, it is straightforward to retain these terms in the derivations.

The momentum and continuity balances for mode-n coefficients are obtained by Galerkin projections, i.e., multiplying (5a) by ϕ_n and (5c) by Φ_n, then using (5b) and (5d), and depth integrating,

$$\frac{\partial \mathbf{U}_n}{\partial t} + \sum_{m=0}^{\infty} \left[(\bar{\mathbf{U}}_{mn} \cdot \nabla) \mathbf{U}_m + (\mathbf{U}_m \cdot \nabla) \bar{\mathbf{U}}_{mn} - (\nabla \cdot \mathbf{U}_m) \bar{\mathbf{U}}_{z,mn} \right] + \mathbf{f} \times \mathbf{U}_n = -H \nabla p_n, \tag{11a}$$

$$\frac{\alpha_n}{g} \frac{\partial p_n}{\partial t} + \sum_{m=0}^{\infty} \left[\frac{\alpha_n}{g} \bar{\mathbf{U}}_{p,mn} \cdot \nabla p_m - \frac{\mathbf{U}_m}{c_n^2} \cdot \bar{\mathbf{B}}_{mn} \right] = -\nabla \cdot \mathbf{U}_n , \tag{11b}$$

where we defined the local variables $\alpha_n \equiv gH/c_n^2$ [a dimensionless scale factor that relates the speeds of surface (mode-0) and internal (mode-n) waves] and $\mathbf{U}_n = H\mathbf{u}_n$ (the equivalent modal transport). These definitions emphasize that the modal momentum equations (11) are a set of "coupled shallow water equations," here associated with vertical modes that are local, i.e., vary in the horizontal. During the derivation of (11), the vertical momentum equation (5b) was used to eliminate b in terms of pressure and, after vertical integration, modal pressure p_n. The continuity equation (5d), also after vertical integration and projection onto modes, was itself used to eliminate the modal vertical velocity in terms of the divergence of the modal transports, i.e.,

$$Hw_m = -\nabla \cdot \mathbf{U}_m \quad \left[\text{m s}^{-1} \right] . \tag{12}$$

Finally, in (11a)–(11b), we defined the "effective mean flow" and "effective mean buoyancy" modal quantities as:

$$\bar{\mathbf{U}}_{mn} = \frac{1}{H} \int_{-H}^{0} \bar{\mathbf{U}} \phi_m \phi_n \, dz \quad \left[\text{m s}^{-1} \right], \tag{13a}$$

$$\bar{\mathbf{U}}_{p,mn} = \frac{1}{H} \int_{-H}^{0} \bar{\mathbf{U}} \frac{N^2}{c_m^2} \Phi_m \Phi_n \, dz \quad \left[\text{m s}^{-1} \right], \tag{13b}$$

$$\bar{\mathbf{U}}_{z,mn} = \frac{1}{H} \int_{-H}^{0} \frac{\partial \bar{\mathbf{U}}}{\partial z} \Phi_m \phi_n \, dz \quad \left[\text{m s}^{-1} \right], \tag{13c}$$

$$\bar{\mathbf{B}}_{mn} = \frac{1}{H} \int_{-H}^{0} \nabla \bar{B} \phi_m \Phi_n \, dz \quad \left[\text{m s}^{-2} \right] . \tag{13d}$$

These quantities correspond to modal interactions and are in general horizontally variable.

From the above results, we remark that the modal internal-tide amplitudes $\mathbf{U}_n$ and p_n are uncoupled when the effective mean flows (13a–13c) and buoyancy (13d) are diagonal. For example, this occurs when $\bar{\mathbf{U}}$ and $\nabla \bar{B}$ are uniform with depth. However, in general, depth-dependent mean flows or mean buoyancy gradients disrupt the orthogonality of the modes, leading to nondiagonal effective mean flows and buoyancy that produce intermodal coupling. For example, a depth-varying mean flow may cause $\bar{\mathbf{U}}_{21} \neq 0$, indicating

that mode-2 velocity amplitudes partially determine the mode-1 velocity amplitude. This latter type of coupling can lead to internal-tide scattering (exchange of tidal energy between different vertical modes) by mesoscale features [e.g., *Dunphy and Lamb*, 2014]. Here more general cases are considered, e.g., we allow depth-dependent N^2 and thus nonsinusoidal vertical modes (9).

The tidally averaged depth-integrated modal energy balances are produced by multiplying (11a) by $\mathbf{u}_n$ and (11b) by p_n, averaging over a tidal period, and summing (this amounts to a dot product, but with the modal pressure and the continuity equation replacing the vertical velocity and vertical-momentum equation, respectively):

$$\nabla \cdot \langle \mathbf{F}_n \rangle + \sum_{m=0}^{\infty} \langle A_{mn} \rangle = \sum_{m=0}^{\infty} \langle P_{mn}^S + P_{mn}^B \rangle . \tag{14}$$

These modal equations (14) can also be obtained by substituting (8) for the total quantities in (7) and then using the result in the full energy equation (6), again for now assuming a flat bottom and rigid lid. In equations (14), the modal-energy flux ($\mathbf{F}_n$), advection of the modal tidal-kinetic-energy by the mean flow (A_{mn}), shear production (P_{mn}^S), and horizontal buoyancy production (P_{mn}^B) are, respectively,

$$\mathbf{F}_n = H \mathbf{u}_n \, p_n = \mathbf{U}_n \, p_n, \tag{15a}$$

$$A_{mn} = \left[(\overline{\mathbf{U}}_{mn} \cdot \nabla) \mathbf{U}_m \right] \cdot \frac{\mathbf{U}_n}{H} + \left(\frac{\alpha_n}{g} \overline{\mathbf{U}}_{p,mn} \cdot \nabla p_m \right) p_n, \tag{15b}$$

$$P_{mn}^S = \left[(\nabla \cdot \mathbf{U}_m) \overline{\mathbf{U}}_{z,mn} - (\mathbf{U}_m \cdot \nabla) \overline{\mathbf{U}}_{mn} \right] \cdot \frac{\mathbf{U}_n}{H}, \tag{15c}$$

$$P_{mn}^B = \left(\frac{\mathbf{U}_m}{c_n^2} \cdot \overline{\mathbf{B}}_{mn} \right) p_n . \tag{15d}$$

They are analogous to the quantities in (7), but here for each internal-tide mode. Once again, the advection term quantifies the transport of tidal energy by the mean flow and the shear-production and buoyancy-production terms quantify energy conversion between the mean flow and the internal tide. However, these advection and production terms also contain modal cross terms (i.e., terms involving combinations of modes n and m), which produce inter-modal energy conversion (i.e., scattering).

2.3. Limitations and Validity

In the derivation of (11) and (14), we assumed sufficiently small-amplitude waves such that we could neglect the instantaneous wave-wave advection terms and their slowly varying averages over a few tidal periods. In doing so, we neglect the fast variability of the nonlinear wave-wave interactions and self-advection, which transfer energy to other frequencies (e.g., tidal harmonics), see for example the studies of *Lamb* [2004], *Legg and Huijts* [2006], *Venayagamoorthy and Fringer* [2006], and *Zhang and Duda* [2013]. Relaxing this assumption would invalidate the monochromatic wavefield solution assumed in (2). The small-amplitude approximation is invalid in regions with large tidal amplitudes, in particular in regions with strong waves and weak mean flows (e.g., shallow shelf with strong tides). Although, deep-ocean internal tides produce much smaller velocities than the those associated with the Gulf Stream. Similarly, in the shelf-break front, the magnitude of the wave-wave advection terms is usually smaller than other terms in (5) and (6)–(7), particularly the mean-flow advection terms. Also, neglecting advection by mean-flow vertical velocities in (11) and (14) limits the theory to hydrostatic dynamics, e.g., to locations where mean flows do not flow up or down steep topographic slopes.

A further limitation of (11) and (14) is that, for a simpler presentation, they were derived assuming a flat bottom. We now discuss how the derivation of these equations can be extended to the case of sloping topographies and how their local interpretation and numerical implementation allows for a zeroth-order treatment of a variable bottom.

First, in the absence of a mean flow, the momentum equations can be corrected by including the topographic coupling coefficients derived by *Griffiths and Grimshaw* [2007]. The coefficients lead to topographic inter-modal energy conversion:

$$C_n = \sum_{m=0}^{\infty} \left[(\mathbf{u}_m p_n) \cdot \int_{-H}^{0} \phi_m \nabla \phi_n \mathrm{d}z - (\mathbf{u}_n p_m) \cdot \int_{-H}^{0} \phi_n \nabla \phi_m \mathrm{d}z \right], \tag{16}$$

which quantifies energy conversion into mode n. The tidally averaged energy balance (6) but with topographic conversion included is then

$$\nabla \cdot \langle \mathbf{F}_n \rangle + \sum_{m=0}^{\infty} \langle A_{mn} \rangle = \langle C_n \rangle + \sum_{m=0}^{\infty} \langle P_{mn}^S + P_{mn}^B \rangle. \tag{17}$$

In the absence of a mean flow, topographic conversion has been shown to balance modal energy-flux divergence over arbitrary topography [*Kelly et al.*, 2012, 2013]. Here we show that C_n explains almost all mode-1 and mode-2 energy-flux divergence along the steep continental slope (sections 5 and 6).

In the presence of a mean flow, topographic effects should, strictly speaking, also be extended to the mean-flow coupling terms themselves. Extending the modal momentum and energy equations to include terms that describe combined mean-flow and topographic coupling is tedious, but straightforward. However, sample calculations of the additional terms in the simulations presented here (not shown) indicate that these additional terms are negligible with respect to the residuals in the momentum and energy balances (i.e., they are less important than viscous and wave-wave terms that are excluded from the balances). Therefore, hereafter we neglect terms that describe the effects of joint topographic and mean-flow coupling, i.e., we only keep all terms in (17).

The sample calculations above also confirm that (11) and (14) can be directly interpreted as a local approximation in the horizontal, i.e., they are utilized column-by-column assuming locally constant depth H and local vertical modes (9). These local equations are then connected in the horizontal through the modal fluxes at the edges of these columns, i.e., through the horizontal gradients in (11a) and (11b), such that all fluxes are conserved as depth and density vary horizontally. The modal-momentum and energy transfers that occur between columns then account for staircase depth variations. In a numerical sense, within a column, a zeroth-order polynomial (a constant) represents the local depth and the vertical modes (9) represent the local vertical variability. When the columns are connected through the tidal equations (11a) and (11b), the result is analogous to a spectral-method representation of the spatially variable bathymetry and tides. When variable topographic terms are added to these local equations as in (17), with or without a mean flow as described above, the result, in the numerical sense, is a higher-order representation of bathymetric effects (e.g., higher-order numerics can then be used for the bathymetric gradients [*Ueckermann and Lermusiaux*, 2010, 2016]).

Next, we discuss how we estimate and postprocess realistic data-driven ocean fields that will be utilized to compute the terms in (11) and (14). This computation later allows the extraction and diagnosis of realistic internal-tide dynamics and interactions.

3. Computation and Implementation

3.1. Data-Driven Numerical Ocean Simulations

Two fully nonlinear numerical models were used to investigate tide-mesoscale interactions. First, the hydrostatic version of the MIT general circulation model (MITgcm) [*Marshall et al.*, 1997] was used to simulate a mode-1 internal tide propagating along and across a realistic two-dimensional cross section of the Gulf Stream. The simulations employ a 2000 km long by 4000 m deep numerical domain with horizontal and vertical grid spacings of 2 km and 20 m, respectively. The incoming internal tide is initiated at the left boundary and has amplitude $u_1 = 0.1 \, \mathrm{m \, s^{-1}}$. Dynamical adjustments at the boundary also produce a mode-2 internal tide that is an order of magnitude weaker.

Next, realistic simulations of tide-mesoscale interaction in the Middle Atlantic Bight region were conducted with the Multidisciplinary Simulation, Estimation, and Assimilation System (MSEAS) [*Haley and Lermusiaux*, 2010; *Haley et al.*, 2015]. Presently, the nonlinear free-surface hydrostatic primitive-equation model of MSEAS is used, in a generalized-level vertical-coordinate configuration. The full domain (shown in Figure 1) is resolved with a 3 km horizontal grid and 100 vertical levels optimized to the thermocline structure. An

implicit two-way nested domain is used over the SW06 shelfbreak with a 1 km horizontal grid. Horizontal velocities are defined along the rotated grid (u is positive to the northeast and v to the northwest).

A "realistic" simulation was initialized with horizontally and vertically variable objectively analyzed meso-scale temperature, salinity, and velocity fields. The objective analyses combine separate analyses inshore and offshore of the expected shelfbreak front using a shelfbreak-front feature model [*Lermusiaux*, 1999; *Gangopadhyay et al.*, 2003], and are multiscale in space [*Lermusiaux*, 2002]. They combine varied in situ synoptic SW06 data (from gliders, conductivity-temperature-depth profiles, autonomous underwater vehicles, etc.) and historical data (from the National Marine Fisheries Service, World Ocean Database, Gulf Stream Feature analyses, Buoy data, etc.). The Gulf Stream was initialized based on in situ and historical CTD profiles and from estimates of its position based on SST and NAVOCEANO feature analyses. Transport-feature models were also used for the Gulf Stream and slope-recirculation gyre. Subgrid-scale parameters were tuned for the region by comparison of hindcasts with independent in situ SW06 measurements. Atmospheric-forcing fluxes were obtained by optimally merging the Weather Research and Forecasting (WRF) fields into the larger Navy Operational Global Atmospheric Prediction System (NOGAPS) fields and applied at the ocean free surface. High-resolution TPXO7.2 surface-tide velocities and elevation, based on [*Egbert*, 1997] but processed for our higher-resolution bathymetry and specific dynamics [*Logutov and Lermusiaux*, 2008; *Haley, et al.*, 2015], were imposed as forcing at the open boundaries. The simulation was initiated on 21 August 2006 and integrated for 42 days, with and without data assimilation. During integration, a novel mixed sponge-open-boundary condition, which relaxes the solution to an exponentially weighted running average, was applied at the lateral boundaries to prevent the reflection of outward-propagating internal tides by absorbing them in a sponge layer, but to allow the free radiation of subtidal fields such as fronts and eddies (P. Haley, personal communication). All of these developments including data processing, external forcing, initialization procedures, data assimilation, and model tuning, as well as the simulated (sub)mesoscale and tidal hindcast and reanalysis fields themselves, will be analyzed in detail and compared with observations in a future manuscript (*Kelly et al.*, personal communication).

To also examine tides without mesoscale variability, a "uniform" MSEAS simulation was initiated with zero mesoscale velocity and horizontally uniform temperature and salinity, which were derived from objectively analyzed offshore observations. The uniform simulation received surface-tide forcing, but not atmospheric forcing.

3.2. Postprocessing of Ocean Fields for Internal-Tide Extraction

To assess the balances in section 2, especially to estimate the terms in (11) and (14), the velocity and pressure fields are first projected onto the local vertical modes obtained from (9) and then Fourier filtered. For the projection step, pressure is determined by (i) calculating density from temperature and salinity, (ii) subtracting the 40 day average density and multiplying by gravity to estimate the buoyancy force, and (iii) vertically integrating the buoyancy force to obtain the pressure field (the constant of integration is determined from the free surface). Hourly time series of three-dimensional horizontal velocity and pressure are then projected onto the local vertical modes to obtain amplitudes for modes $n = 0$ to $n = 10$. The modes and eigenspeeds at each horizontal location are obtained by numerically solving the relevant eigenvalue problem (9) using second-order-accurate finite differences. Mode-0 is approximated as: $\phi_0 = 1$ and $c_0 = \sqrt{gH}$.

For the Fourier step, the hourly time series of modal velocities are broken into fifteen 62 h segments (i.e., five M_2 tidal periods; the first 62 h during spin-up are discarded) and Fourier transformed. The resulting Fourier coefficients have a spectral resolution of about 0.4 cycles per day (cpd). The semidiurnal (1.93 ± 0.2 cpd) Fourier coefficients vary between segments because of (i) changes in surface-tide forcing (i.e., the spring-neap cycle) and (ii) modulation by rapidly evolving mesoscale features. Variability due to (i) and (ii) are separable by their coherence and noncoherence [*Munk and Cartwright*, 1966; *Kelly et al.*, 2015], respectively, with TPXO surface-tide elevations. Here coherent and noncoherent motions are defined as the average of the coherent Fourier coefficients from all of the 62 h segments (i.e., the ensemble average) and their residuals, respectively. Coherent energy is computed from the coherent Fourier coefficients and noncoherent energy is defined as total energy minus coherent energy [e.g., *Munk and Cartwright*, 1966; *Kelly et al.*, 2015]. Because tide-mean-flow interactions are often weak and their numerical computation can be noisy, here we analyze the dynamics of the coherent ("stationary") internal tide, which are much more accurately computed than those of the noncoherent internal tide.

Coupling coefficients (13a) and (13d) are also obtained from the three-dimensional flow and buoyancy fields of the realistic MSEAS primitive-equation simulations, along the rotated grid. Mean flows are defined as the time averages over each 62 h period. The "effective mean flows" are then numerically computed for each time period at each location using the local modes. Horizontal gradients are computed using a centered difference at the model grid scale. Topographic conversion is calculated following *Kelly et al.* [2012]. The mean-flow vertical shear terms are computed using the integral

$$\int_{-H}^{0} \frac{\partial \overline{\mathbf{U}}}{\partial z} \Phi_m \phi_n \mathrm{d}z = \int_{-H}^{0} \overline{\mathbf{U}} \left(\Phi_m \Phi_n \frac{N^2}{c_n^2} - \phi_m \phi_n \right) \mathrm{d}z , \qquad (18)$$

which is derived using integration by parts. Summations of the energy-conversion terms in (14) are truncated at $m = 10$. Check-calculations indicate that contributions from higher modes are negligible. The tide-mean-flow interaction terms for the coherent tide are computed using the coherent tidal amplitudes (i.e., ensemble-averaged amplitudes over all 62 h periods) and the mean flows from each 62 h period.

4. Idealized Simulations

MITgcm simulations of a mode-1 internal tide propagating across and along the Gulf Stream (section 3.1) are used to examine the energy balance (14; Figure 2). In the simulation of across-stream propagation, the inertial frequency is consistent with 40°N and the idealized Gulf Stream is in geostrophic balance. When the incoming mode-1 internal tide hits the Gulf Stream it encounters a deeper pycnocline and obtains a longer wavelength and deeper zero crossing (Figure 2a). It also gains energy though shear production and loses energy through buoyancy production (Figure 2c), producing approximately zero net energy conversion and energy-flux divergence (Figure 2e).

In the simulation of along-stream propagation, the inertial frequency is set to zero and the Gulf Stream is driven by inflow/outflow conditions at the boundaries. Neglecting the Coriolis force allows the flow to be
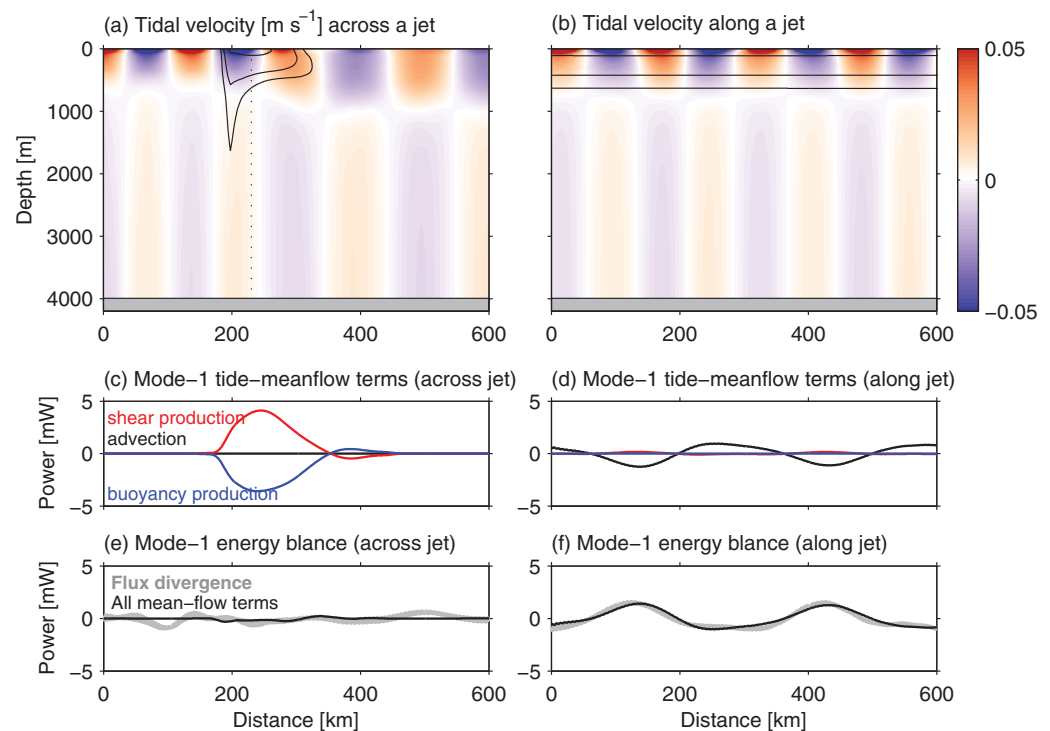

Figure 2. (a) Horizontal internal-tide velocity in idealized MITgcm simulation (section 3.1) of a mode-1 tide propagating from left to right across and (b) along a cross section of a steady Gulf Stream. Contours indicate 0.5, 1, and 1.5 m s^{-1} mean-flow velocities (into the page or to the right). Mode-1 energy advection, shear production, and buoyancy production terms are shown in Figures 2c and 2d. The total mode-1 energy-flux divergence and mean-flow conversion are shown in Figures 2e and 2f. Advection was moved to the right-hand-side of (14) when calculating total mean-flow conversion.

represented in two dimensions (along-stream and vertical). In this simulation, the incoming mode-1 internal tide periodically gains and loses energy due to advection by the mean flow (Figure 2d), which balances mode-1 energy-flux divergence (Figure 2f). Energy advection (15b) depends on spatial gradients of wave velocity and pressure; however, the background conditions in this simulation do not introduce any stream-wise variability in the internal tide. Instead, the advection term arises because imperfect boundary conditions generate a small mode-2 internal tide, which facilitates three-way interactions between the mean flow and the mode-1 and mode-2 tides. The horizontal periodicity in the energy advection term arises because of the phasing of the mode-1 and mode-2 internal tides. Inspection of the mode-2 energy balance (not shown) reveals much smaller advection effects (i.e., $A_{21} \gg A_{12}$), suggesting that in this simulation the modal interaction primarily mediates energy advection, not energy transfer between modes.

5. Internal-Tide Coherence and Generation in the Middle Atlantic Bight Region

We now study the effects of mean flows and horizontally variable stratification on internal tides in the MSEAS primitive-equation numerical simulations (section 3.1). The realistic simulation has energy at a continuum of frequencies between $\omega = 0-2$ cpd (Figures 3a–3c). The shelfbreak front and Gulf Stream, which are permanent baroclinic features, produce an energy peak at $\omega = 0$ cpd, which extends over all vertical modes. Wind-driven inertial oscillations produce an energy peak at $\omega = 1.2$ cpd (19 h period), which extends over modes 1–8. The semidiurnal tide produces an energy peak at $\omega = 2$ cpd, which is dominated by modes 0 and 1 (i.e., the surface tide and mode-1 internal tide).

Coherent-energy peaks in the MSEAS simulations are associated with the surface tides (vertical mode-0) and the mode-1 semidiurnal internal tide. Noncoherent-energy peaks are associated with variable mean flows, intermittent wind-driven oscillations, and nonstationary semidiurnal internal tides. These noncoherent features are largely absent in the "uniform" MSEAS simulation (Figures 3d–3f), which has much weaker mean flows, no near-inertial oscillations, and primarily stationary internal tides.
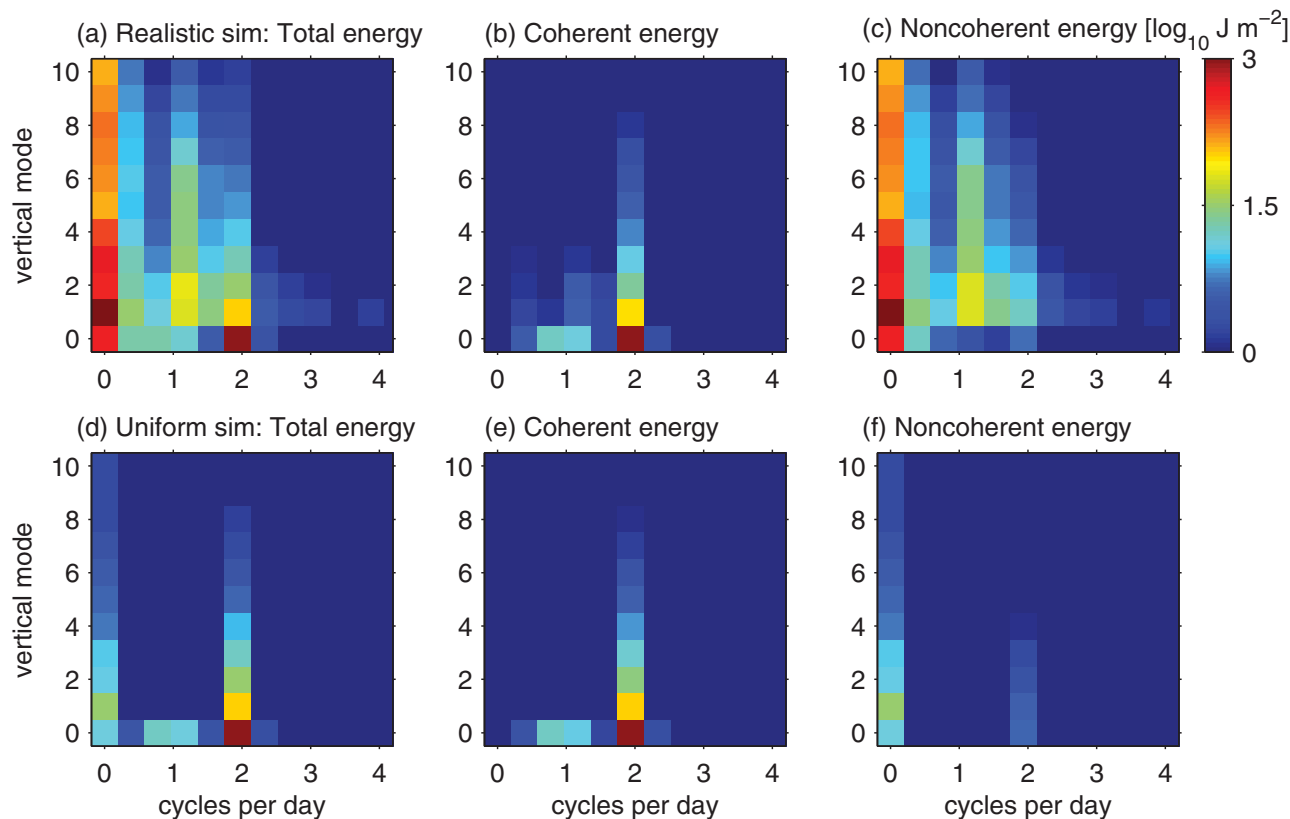

Figure 3. Total energy in two MSEAS primitive-equation simulations (section 3.1) decomposed by frequency and vertical mode. The realistic MSEAS simulation (a–c) has energy at a continuum of frequencies, which is both coherent and noncoherent with the surface tide. The "uniform" MSEAS simulation (d–f) has mostly coherent tidal energy.
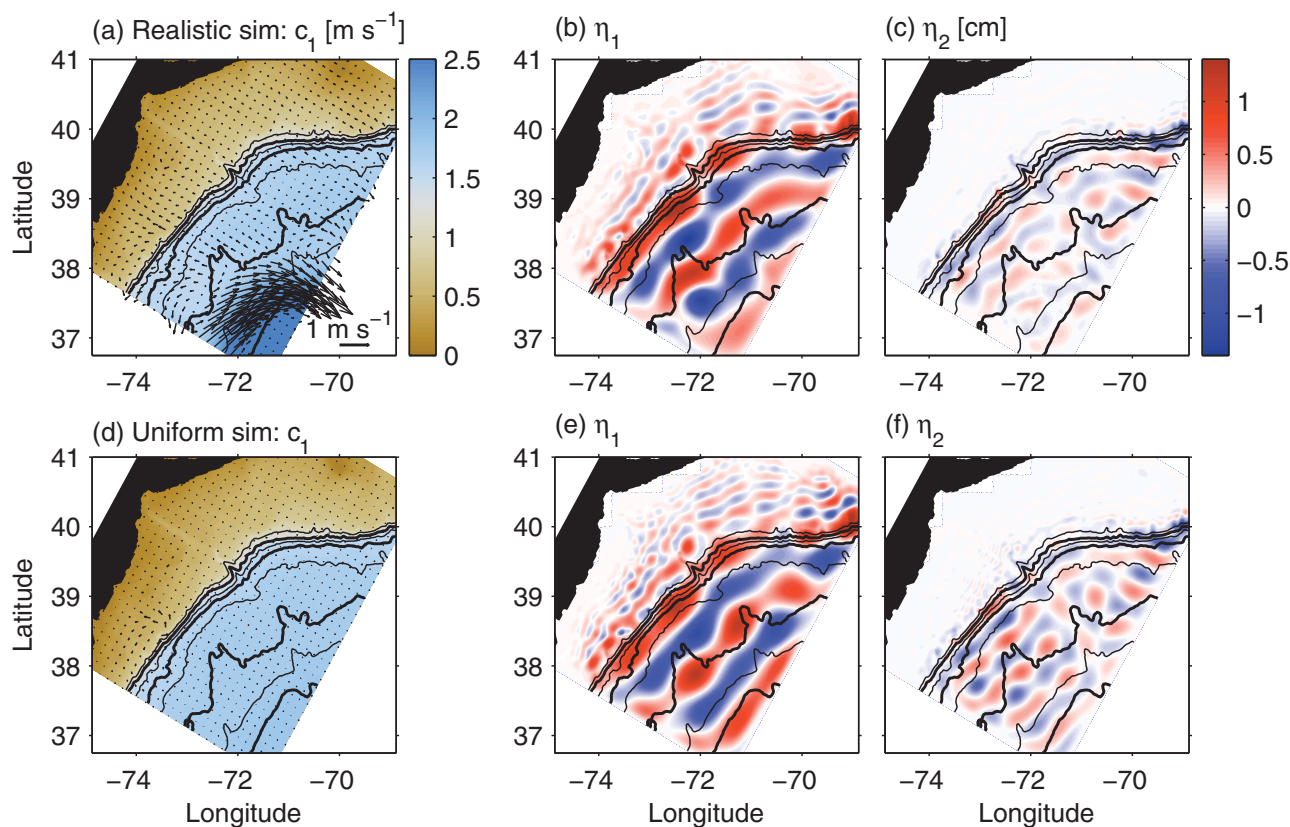
Figure 4. Forty-two-day average of mode-1 eigenspeeds and surface velocity for the (a) realistic and (d) uniform simulations. Snapshots at 02:48 1 September 2016 of the mode-1 and mode-2 surface displacements from the (b and c) realistic and (e and f) uniform simulations.

Maps of mode-1 eigenspeed and mean surface currents in the uniform and realistic simulations illustrate the effect of the summer shelf, shelfbreak front and Gulf Stream on the internal-tide waveguide (Figures 4a and 4d). Although eigenspeeds are similar in both simulations because eigenspeed is primarily a function of depth, eigenspeeds increase in the strong stratification associated with the Gulf Stream and, to a lesser extent, on the shelf due to the presence of a shelfbreak front and strong summer shelf stratification.

In both simulations, snapshots of coherent semidiurnal mode-1 and mode-2 sea-surface displacements [i.e., $\eta_n = p_n \phi_n (z=0)/g$] display internal-tide fronts radiating from the shelfbreak (Figures 4b, 4c and 4e, 4f). The mode-1 tide has significantly larger amplitude than the mode-2 tide (although mode-2 tides are slightly more energetic in the uniform simulation than the realistic simulation due to enhanced shelfbreak generation; see section 6.1). In the realistic simulation, the shape and amplitude of the wave fronts in the southern portion of the domain are distorted due to interactions with the Gulf Stream. In addition, mode-1 wavelengths on the shelf are slightly longer in the realistic simulation than the uniform simulation because the shelfbreak front and realistic summer shelf correspond to an increased stratification on the shelf. Also, in the realistic simulation, the detailed internal-wave patterns on the shelf are clearly modified, e.g., by (sub)-mesoscale features at the front and also by wind-driven upwelling, currents and eddies within the inner-shelf and at the coast.

Mode-1 and mode-2 energy balances in the realistic simulation reveal that most energy-flux divergence is balanced by topographic internal-tide generation at the shelfbreak (Figure 5). Throughout much of the domain, the traditional residuals (i.e., $C_n - \nabla \cdot \mathbf{F_n}$) are small and positive, consistent with weak numerical dissipation. However, residuals are larger in some regions, mainly because wave-mean-field interaction terms are needed to close the local energy budget. Energy balances in the realistic and uniform simulations are almost identical, except at the shelfbreak front and certainly at the Gulf Stream (on the shelf, relative differences are significant but absolute differences are much smaller). At the Gulf Stream, the mean flow produces a pattern of mode-1 energy-flux convergence and divergence that cannot be explained by
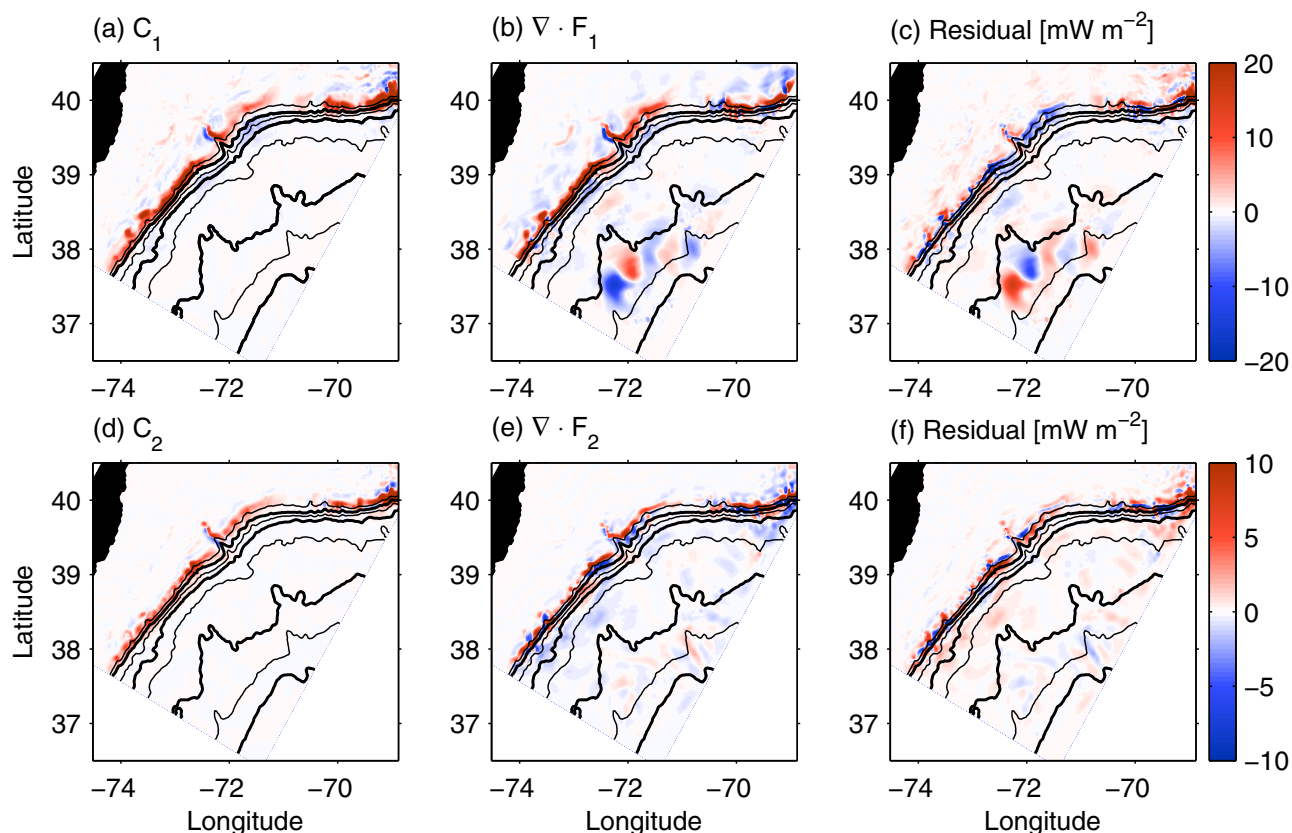
Figure 5. (a) In the realistic simulation, 42 day average mode-1 and (d) mode-2, topographic energy conversions are balanced by energy-flux divergences (b and e). For each mode ($n = 1, 2$), the traditional residual field, $C_n - \nabla \cdot \mathbf{F_n}$, is shown in Figures 5c and 5f. Small positive residuals imply viscous dissipation, while large positive/negative residuals indicate regions where nonlinear and/or mean-flow effects are important (e.g., near the Gulf Stream in the realistic simulation and also near the shelfbreak front, as seen in Figure 5c). These residuals correspond to terms the new theory explains.
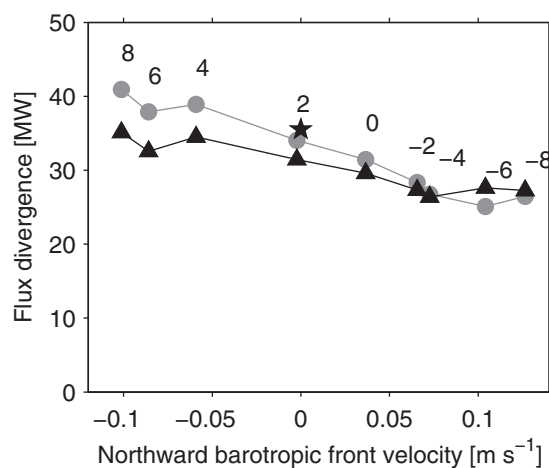
Figure 6. Energy-flux divergence (circles) and conversion (triangles) at the SW06 shelfbreak (62 h average centered around August 27, and integrated inside the box in Figure 1) decreases as the northward barotropic mean flow increases. The numbers indicate the amount the shelf water was warmed in degrees Celsius. The star indicates energy-flux divergence from the uniform simulation, which does not contain a shelfbreak front.

topographic generation or by viscous dissipation. Because offshore mode-1 surface displacements and energy-flux divergences are much larger than those associated with mode-2, we primarily focus on mode-1 dynamics in the Gulf Stream. Because abrupt topography generates high-mode internal tides, we examine total internal-tide energy flux $\mathbf{F}$ and conversion C (i.e., F_n and C_n summed over modes $n = 1$–10) at the shelfbreak.

6. Tidal Interactions With the Shelfbreak Front

6.1. Energy Balance

The presence of the realistic shelfbreak front reduces total energy-flux divergence $\nabla \cdot \mathbf{F}$ at the SW06 study site by about 10% in the realistic simulation with respect to the uniform simulation on 27 August (Figure 6). To test whether
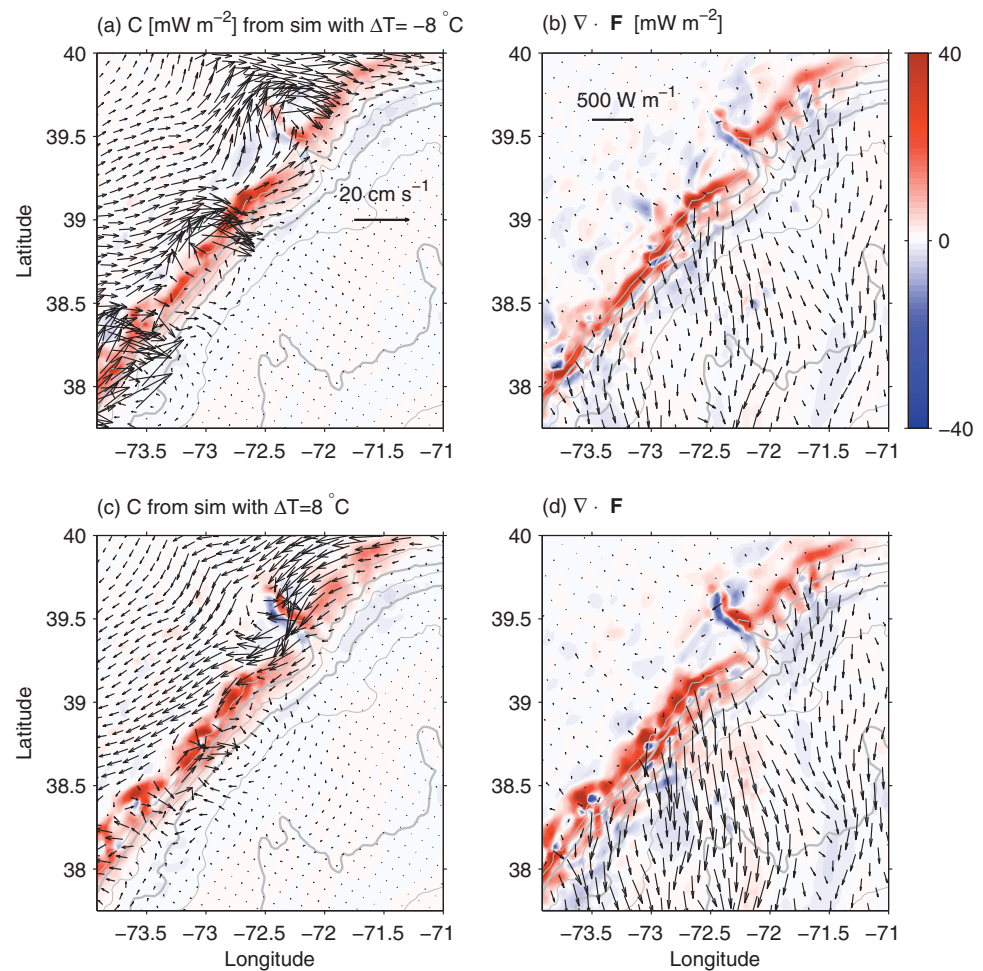
Figure 7. Internal-tide generation (62 h average centered around August 27) is weaker when the shelf water is (a) cooled instead of (c) warmed, but remains roughly balanced by energy-flux divergence at the larger along-front scales, in either case (b and d). Vectors in Figures 7a and 7c are barotropic flow velocities. Vectors in Figures 7b and 7d are internal-tide energy fluxes.

this trend extends to stronger fronts, we conducted eight additional MSEAS simulations, where shelf water in the realistic simulation was uniformly warmed by -8, -6, -4, -2, 2, 4, 6, and 8°C, a range of temperatures that is larger than commonly observed [the observed temperature difference across the front, which varies with season, is ~2–6°C; *Linder and Gawarkiewicz*, 1998]. Warming the shelf water enhances southward flow, which is normally observed at the front, while cooling the shelf water produces northward flow. Cooling the shelf water, which tilts the isopycnals more towards the same direction as the bathymetric slope, decreases $\nabla \cdot \mathbf{F}$ and, to a lesser extent, total topographic internal-tide conversion, C, as qualitatively predicted by *Chuang and Wang* [1981]. The difference in energy-flux divergence between the extreme cold and warm-shelf anomaly simulations is about 40%, indicating the shelfbreak front can produce significant changes in internal-tide generation.

In the anomaly simulations, C overall decreases as the shelf water is cooled, explaining roughly 2/3 of the decrease in $\nabla \cdot \mathbf{F}$. Even in the extreme cold and warm-shelf anomaly simulations, C and $\nabla \cdot \mathbf{F}$ maintain a rough balance (Figure 7). In many of the simulations C is slightly less than $\nabla \cdot \mathbf{F}$, indicating a small unidentified source of internal-tide energy, potentially due to nonlinear topographic generation and/or combined topographic-mean-flow coupling (section 2.3). Overall, in the shelfbreak region, the mean-flow terms derived here (15b–15d) are relatively small (not shown) at the larger along-front scales. For the buoyancy production, this is in part because the local modal transport and modal buoyancy gradient are close to being orthogonal at the front. At these larger shelfbreak front scales, the dominant balance between topographic conversion and energy-flux divergence implies that the overall effect of the shelfbreak front is
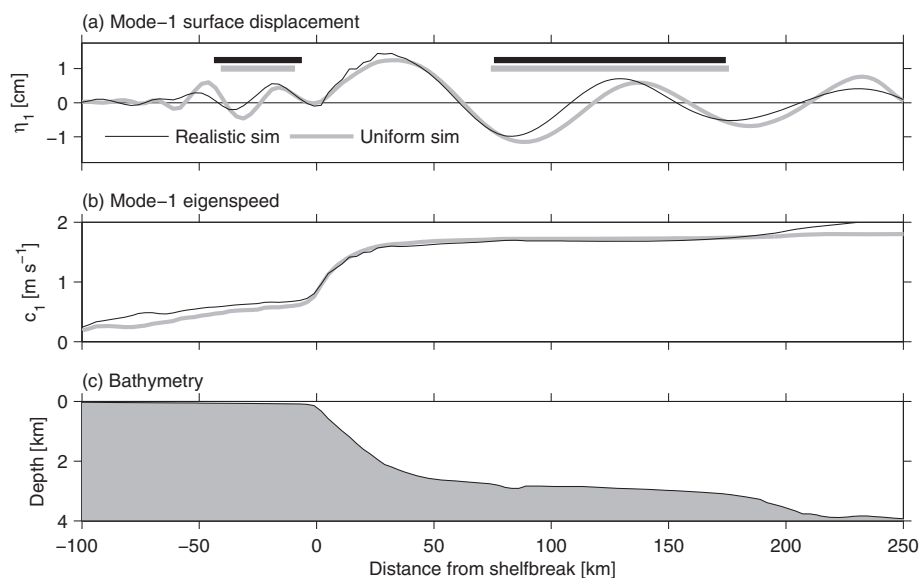
Figure 8. Across-slope snapshots at 02:48 1 September 2016 of mode-1 surface displacement indicate different wavelengths in the realistic (black) and uniform (gray) MSEAS primitive-equation simulations. (b) The simulated wavelengths agree with theoretical wavelengths (bars) determined from 42 day average eigenspeeds. The bathymetry is shown in Figure 8c.

largely captured by the effect of stratification on topographic coupling; stratification alters the horizontal gradients of the modes, ϕ_n, that are used to compute C_n (16). *Kurapov et al.* [2010] described a similar situation on the Oregon Slope, where wind-driven upwelling altered stratification and hence topographic coupling and internal-tide generation. In both locations, the effect of stratification on generation may be qualitatively explained by stratification altering slope criticality.

Considering now the local (sub)mesoscales in the shelfbreak region, the mean-flow terms derived here (15b–15d) are not everywhere negligible (not shown), as indicated by residuals in Figure 5 and imbalances in Figure 7. Hence, mean-flow and buoyancy variability are important at smaller internal-frontal scales, e.g., involving frontal meanders, eddying, or variations in the tilt of the front [*Lermusiaux*, 1999; *Colosi et al.*, 2001; *Gawarkiewicz et al.*, 2001; *Kelly et al.*, personal communication]. For detailed wave studies and forecasts at the front, the effects of mean-flow advection, shear, and horizontal buoyancy gradients would need to be simulated explicitly. We note that nonlinear wave-wave advection could then also become significant, e.g., where internal waves steepen.

6.2. Horizontally *Varying* *Stratification*
The shelfbreak front arises because of large horizontal variations in density, which alters stratification and internal-tide propagation. During SW06, the summer stratification produced a shallow pycnocline on the shelf, leading to stronger stratification, higher eigenspeeds, and longer-wavelength internal tides (Figure 8). Hence, the realistic simulation has both longer-wavelength internal tides on the shelf and shorter-wavelength internal tides in the abyss than the uniform simulation. A simulation with horizontally uniform stratification cannot simultaneously produce the correct wavelengths over both the shelf and abyss. A practical implication of this result is that mode-1 internal tides that are generated at the shelfbreak arrive at a point 40 km onshore of the shelfbreak about 4 h later in the uniform simulation than the realistic simulation. Such variability is thus critical for internal-tide forecasting [e.g., *Duda et al.*, 2014b] (*Kelly et al.*, personal communication).

7. Tidal Interactions With the Gulf Stream

7.1. Momentum *Balances*
Mode-1 internal tides propagate as a linear shallow-water inertia-gravity waves; therefore, in equation (11a), their momentum tendency (which also includes the Coriolis force) is primarily balanced by their pressure-gradient force (Figures 9 and 10). For example, the *v*-momentum balance (Figure 10) reveals alternating
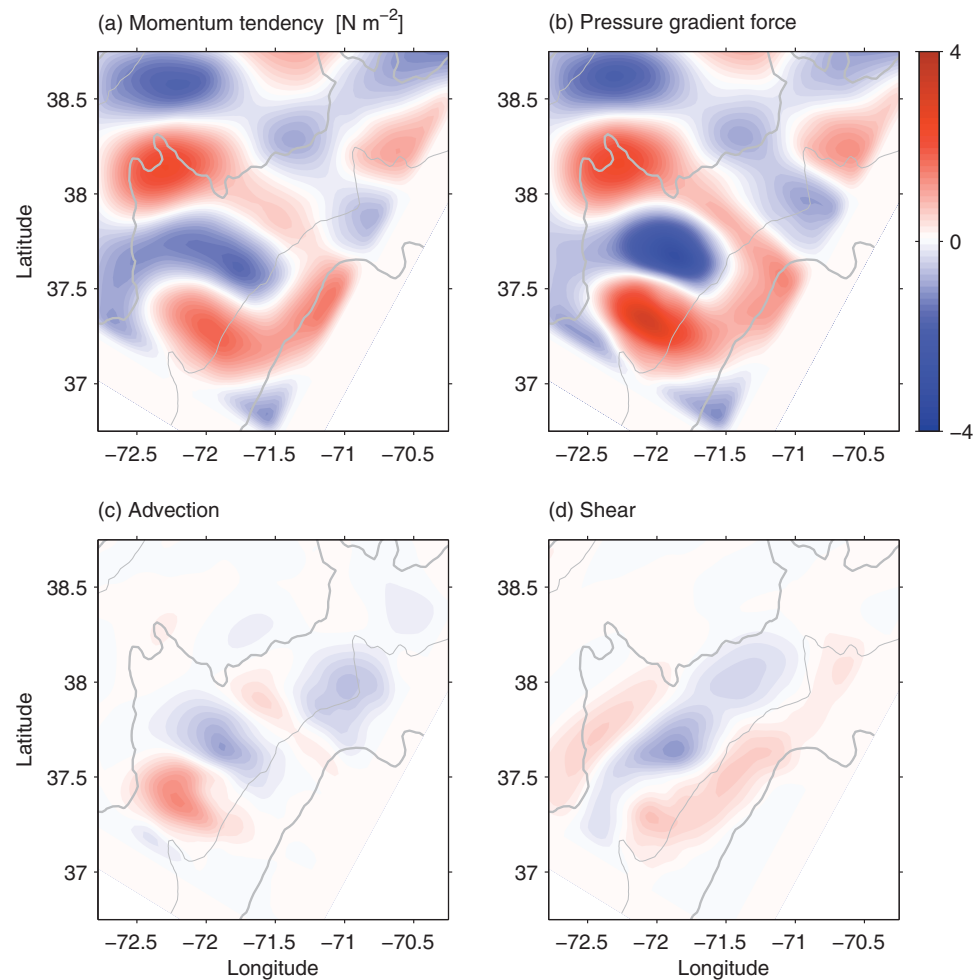
Figure 9. The mode-1 u-momentum balance [see equation (11a)], where u is positive to the northeast along the rotated MSEAS-model grid (i.e., $u \sim$ alongshelf). Terms are computed using semidiurnal Fourier coefficients and time-averaged mean flows from each 62 h period. The terms are then ensemble averaged over all 62 h periods and plotted at an arbitrary phase. Clockwise: the wave-momentum tendency (a) includes the Coriolis force, $\rho_0(\partial U_1/\partial t - fV_1)$; the wave-pressure-gradient force (b) is $-\rho_0 H \partial p_1/\partial x$; the advection of wave momentum by the mean flow (c) is $\rho_0 \sum_m (\bar{\mathbf{U}}_{m1} \cdot \nabla) U_1$; and, the interactions of waves with background shear (d) are $\rho_0 \sum_m [(\mathbf{U}_m \cdot \nabla)\bar{U}_{m1} - (\nabla \cdot \mathbf{U}_m)\bar{U}_{z,m1}]$.

bands of positive and negative pressure-gradient forcing that correspond to the back and front of southeast-propagating internal-wave crests (note that v is positive to the northwest). Each region of strong pressure-gradient forcing produces a fluid acceleration (i.e., momentum tendency).

Likewise, in equation (11b), the evolution of their surface displacement (i.e., pressure tendency) is primarily determined by wave-induced horizontal-velocity convergence (Figure 11). Specifically, horizontal velocities converge and pressure increases prior to the passage of a wave crest. Together, the v-momentum and pressure balances (Figures 10 and 11) are consistent with freely propagating waves, where surface displacement and velocity in the direction of wave propagation (and their tendencies) are in phase (again, note that v is positive to the northwest).

However, in the Gulf Stream, where the slowly varying mean flows exceed 1 m s^{-1}, tide-mean-flow interactions (e.g., advection, shear, and buoyancy terms) are found to explain $\mathcal{O}(10\%)$ of the momentum and pressure tendencies. For example, u-momentum (which is positive to the northeast; Figure 9c) and pressure (Figure 11c) are noticeably advected by the Gulf Stream. Although the wave-mean-flow terms are small compared to the pressure-gradient force and velocity convergence, they explain the largest deviations from the typical shallow-water-wave momentum balances (Figure 12), indicating that background-flow effects
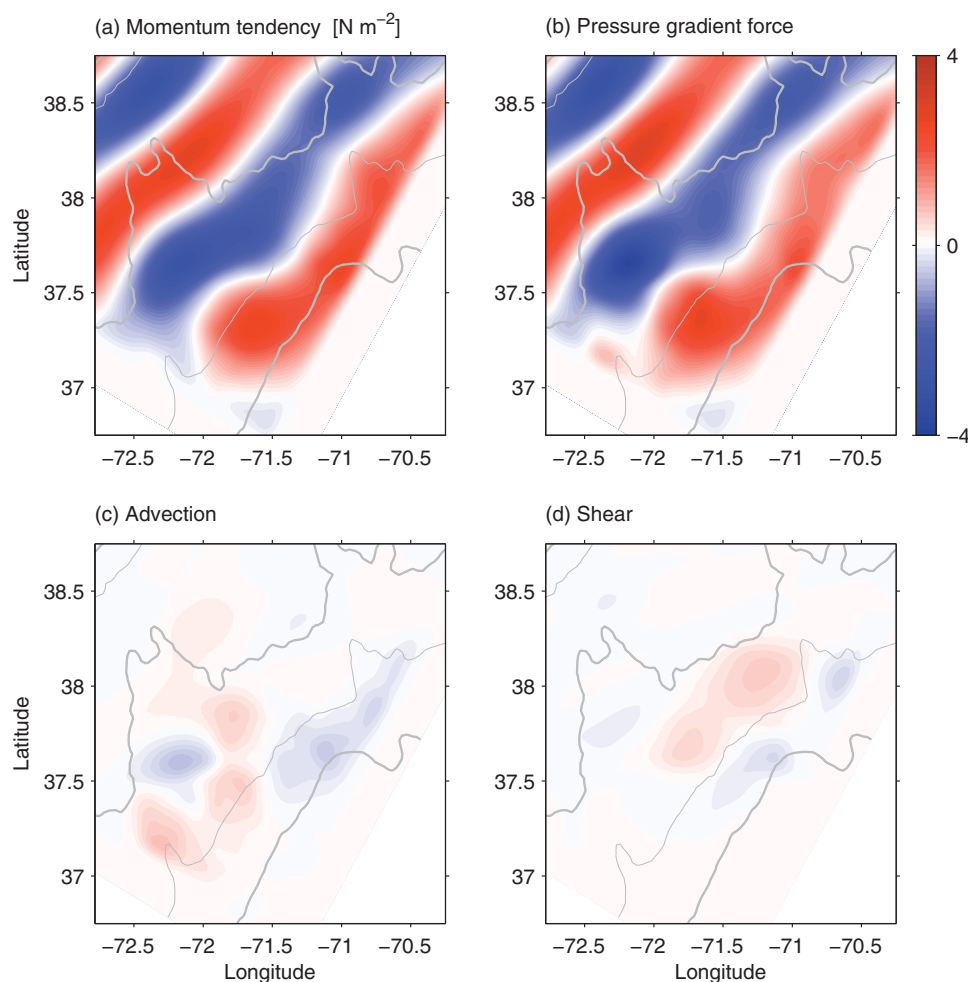
Figure 10. As Figure 9, but for the mode-1 v-momentum balance [see equation (11a)], where v is positive to the northwest along the rotated MSEAS-model grid (i.e., $v \sim$ acrosshelf).

have a larger impact on local deep-ocean simulated mode-1 tidal dynamics than topographic, dissipative, or wave-wave interactions.

7.2. Energy Balance

The Gulf Stream is associated with regions of $\mathcal{O}(20 \text{ mW m}^{-2})$ anomalous mode-1 internal-tide energy-flux convergence and divergence (Figure 5). These anomalies are explained by tide-mean-flow terms in the mode-1 energy balance, which indicate that mode-1 energy is advected by the mean flow and, to a lesser extent, transformed by mean-flow shear and buoyancy production (Figure 13). The spatial distribution of total mean-flow energy conversion closely matches that of mode-1 energy-flux divergence (Figure 14), indicating the local importance of tide-mean-flow interactions.

The spatial patterns of the individual energy terms in the realistic simulation are also similar to those in the two-dimensional idealized simulations; e.g., shear production is balanced by buoyancy production where the mode-1 tide crosses the Gulf Stream (c.f. Figures 2c and 13c, 13d), and advection is large and horizontally periodic where the mode-1 tide propagates against the Gulf Stream (Figure 15).

7.3. Refraction and Reflection

The energy balances derived in section 2 allow for internal-tide scattering by the mean flow and internal-tide interactions with horizontal and vertical mean-flow shear. However, the dominant source of mode-1 energy-flux divergence in the Gulf Stream is mostly advection by the mean flow (Figures 13 and 14). This finding may seem surprising because the mode-1 internal tide and Gulf Stream do not have a clear
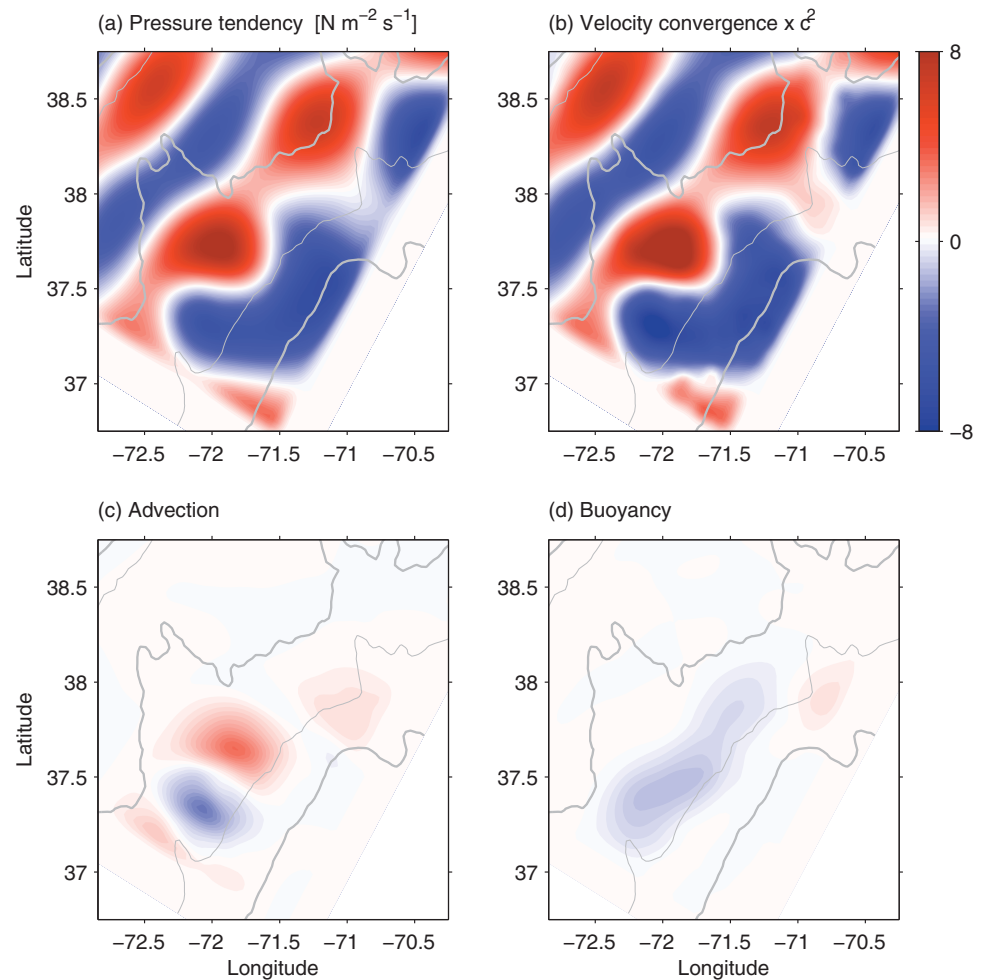
Figure 11. As Figure 9, but for the mode-1 pressure balance [see equation (11b)]. Clockwise: the wave-pressure tendency (a) is $\rho_0 \partial p_1 / \partial t$; the wave-velocity convergence (b) is $-\rho_0 c_1^2 \nabla \cdot \mathbf{u}_1$; the advection of wave pressure by the mean flow (c) is $\rho_0 \sum_m \overline{\mathbf{U}}_{p,m1} \cdot \nabla p_m$; and, the interaction of waves with horizontal-gradients in the mean buoyancy (d) is $-\rho_0 \sum_m \mathbf{u}_m \cdot \overline{\mathbf{B}}_{m1}$.

horizontal-scale or vertical-scale separation. However, the result attests to strong and slowly varying advection of the tide by the Gulf Stream (within its core, the advection is relatively uniform). Next, we exploit this empirical finding by using geometric wave theory to predict how internal-tide propagation is altered by advection in the Gulf Stream. Further analysis [S. M. Kelly, A coupled-mode shallow water model for tidal analysis: Internal-tide reflection and refraction by the Gulf Stream, submitted to *Journal of Physical Oceanography*, 2016; hereafter *Kelly et al.*, 2016] confirms these first-order predictions using a linearized internal-tide model that incorporates mean-flow shear, horizontal-buoyancy gradients, and advection (i.e., their simulations confirm that mean-flow shear does not significantly alter mode-1 internal-tide propagation in the Gulf Stream). Of course, accurate and detailed tidal predictions require direct primitive-equation simulations of all the instantaneous nonlinear interactions described in section 2.

7.3.1. Geometric Wave Theory for Refraction and Reflection

A plane wave that propagates from a quiescent fluid into a mean flow in the *y* direction, $V(x)$, will conserve absolute frequency (the frequency measured from a fixed instrument), ω, and its along-stream wave number, *l*, provided the flow is invariant in the *y* direction. By linearizing the material derivative (i.e., applying geometric wave theory, which neglects mean-flow shear), the phase speed of the wave can be written $c_p = (\omega - Vl)/\kappa$, where $\kappa = \sqrt{k^2 + l^2}$ is the magnitude of the wave number and phase speed is related to eigenspeed by $c_p = c_n / \sqrt{1 - f^2/\omega^2}$ [see e.g., *Alford and Zhao*, 2007]. This expression for phase speed is equivalent to the equation describing Doppler shifting $\hat{\omega} = \omega - Vl$, where $\hat{\omega}$ is the intrinsic frequency [the frequency measured by an instrument moving with the mean flow; *Bühler*, 2009].
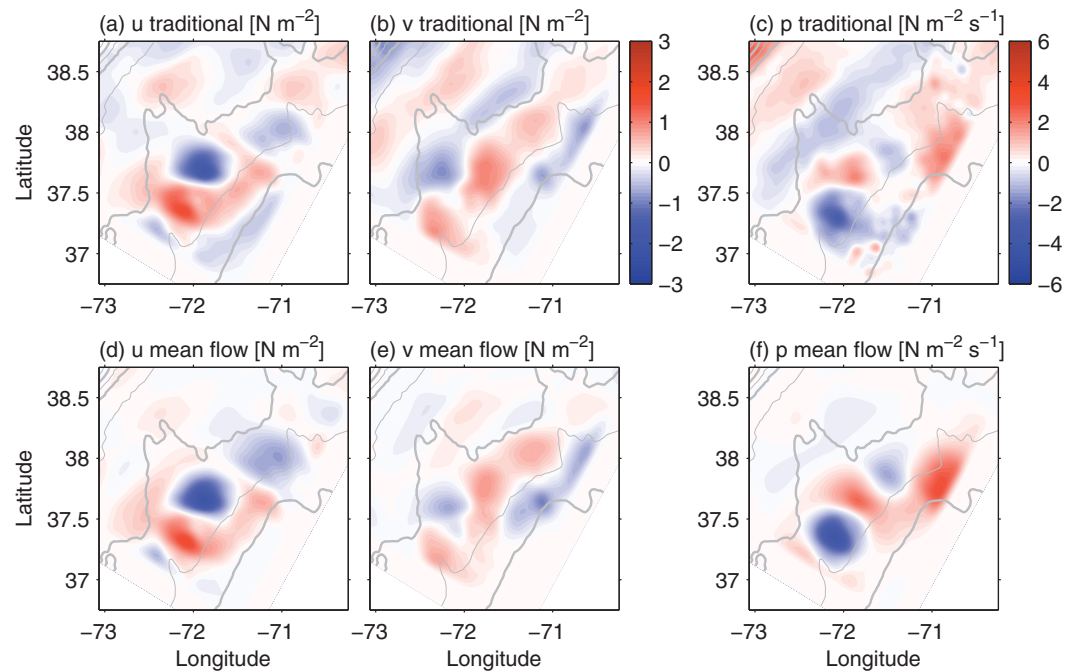
Figure 12. (top row) Residuals of the (a) "traditional" u-momentum, (b) v-momentum, and (c) pressure balances, defined as the u/v-momentum tendency minus the pressure-gradient force and the pressure tendency minus the velocity convergence, respectively. Bottom row: the sums of all tide-mean-flow interaction terms in the (d and e) momentum and (f) pressure balances (see Figures 9–11). (top row) Clearly, these sums of the new "effective mean flow" and "effective mean buoyancy" terms [equation (13)] closely resemble the residuals of the traditional balances. They are the leading-order missing terms and a key result of our derivations. Note that velocities and gradients are still defined for the rotated MSEAS-model grid.

To predict refraction, we solve for changes in the across-stream wave number k, for given ω, V, c_p, and initial wave vector (k_i, l). Setting the initial and final absolute frequencies equal to each other produces:

$$c_{pi}\kappa_i = c_{pf}\kappa_f + Vl , \qquad (19)$$

which simplifies to

$$\frac{c_{pi}}{c_{pf}} - \frac{V}{c_{pf}}\cos\theta = \frac{\kappa_f}{\kappa_i} , \qquad (20)$$

where i and f subscripts denote initial and final values, respectively, and θ is the angle of the incident wave with respect to the mean flow (i.e., when $\theta = 90°$, the wave propagates directly across the flow). Since l is fixed, any increase in κ_f/κ_i implies refraction due to changes in across-stream wave number. For example, when $V = 0$, a wave propagating into a coastal region with $c_{pf} < c_{pi}$ increases across-stream wave number and turns towards shore. Conversely, when phase speed is constant ($c_{pf} = c_{pi}$) and $0 < V < c_{pf}$, a wave propagating into a following current ($0 < \theta < 90°$) will turn to propagate with the current. A wave propagating into an opposing current ($90 < \theta < 180°$) will turn to propagate across the current. A wave propagating perpendicular to a current ($\theta = 90°$) does not refract.

In some flows, the final along-stream wave number must be imaginary to satisfy (20), indicating that the incident wave is reflected. The condition for reflection is:

$$\left(\frac{c_{pi}}{c_{pf}} - \frac{V}{c_{pf}}\cos\theta\right)^2 < \cos^2\theta . \qquad (21)$$

Without a mean flow ($V = 0$), reflection is possible when a wave propagates from shallow to deep water ($c_{pi} < c_{pf}$) at a nonnormal angle ($\theta \neq 90°$), as shown by *Chapman and Hendershott* [1981]. When phase speed is constant ($c_{pf} = c_{pi}$) and $0 < V < c_{pf}$, waves propagating into a following current ($\cos\theta > 0$) are more likely to reflect than those propagating into an opposing current ($\cos\theta < 0$).
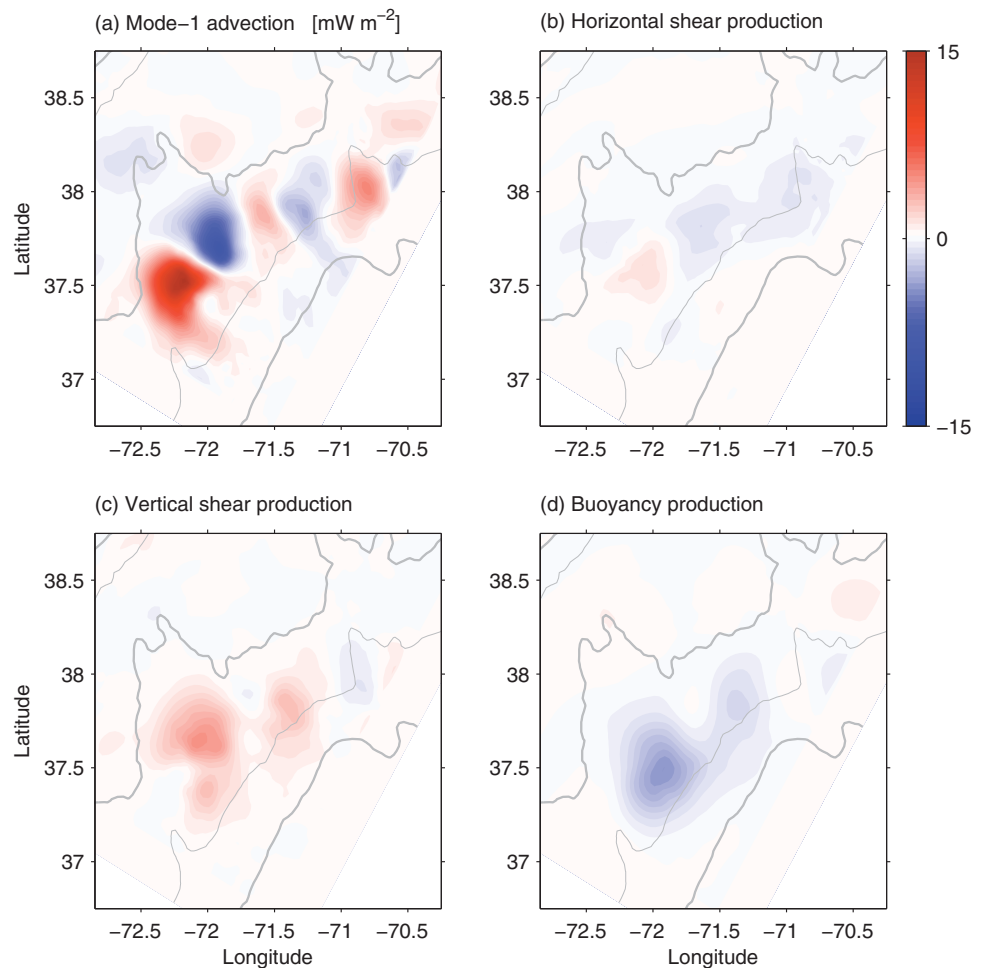
Figure 13. Mode-1 energy balance [see equation (17)]. The terms that are all enhanced in the Gulf Stream are [see equation (15)]: the modal tidal-energy advection by the mean flow (a), $\sum_{m=0}^{10} \langle A_{m1} \rangle$; vertical-shear production (c), $\sum_{m=0}^{10} \langle [(\nabla \cdot \mathbf{U}_m)\overline{\mathbf{U}}_{z,m1}] \cdot \frac{\mathbf{U}_1}{H} \rangle$; and buoyancy production (d), $\sum_{m=0}^{10} \langle P_{m1}^B \rangle$. The horizontal-shear production (b), $-\sum_{m=0}^{10} \langle [(\mathbf{U}_m \cdot \nabla)\overline{\mathbf{U}}_{m1}] \cdot \frac{\mathbf{U}_1}{H} \rangle$, is a bit weaker than the other terms.
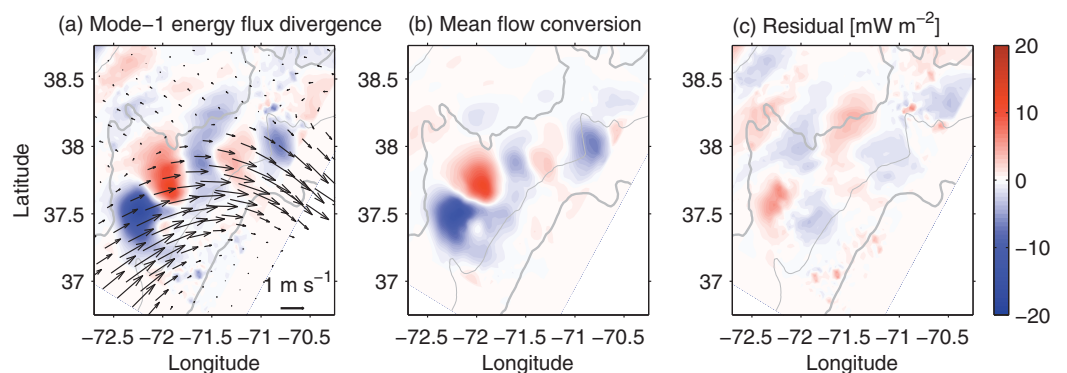
Figure 14. In the Gulf Stream, the pattern of mode-1 energy-flux divergence (a), $\nabla \cdot \langle \mathbf{F}_n \rangle$, is explained by the sum of all tide-mean-flow energy conversion terms (b), $\sum_{m=0}^{10} \langle P_{m1}^S + P_{m1}^B - A_{m1} \rangle$. (c) Their difference, i.e., the residual of the energy-flux divergence and tide-mean-flow energy-conversion terms, is an order of magnitude smaller. (a) Vectors represent surface mean-flow velocities associated with the Gulf Stream.
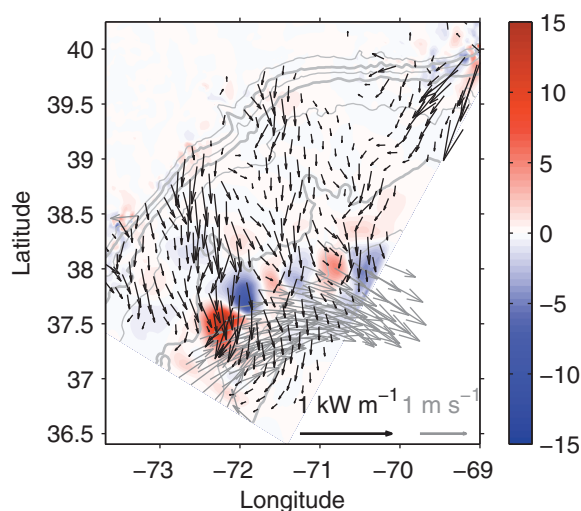
Figure 15. Mode-1 energy advection (W m^{-2}, red/blue coloring) is enhanced where mode-1 energy flux (black vectors) strikes the Gulf Stream (initial surface velocities are denoted by gray vectors).
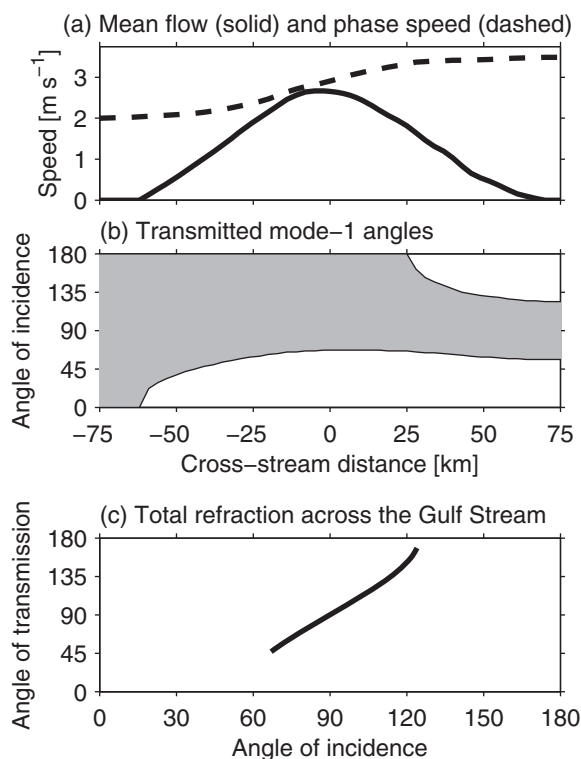

Figure 16. (a) The cross-stream profile of the Gulf Stream has velocities $\bar{U}_{11} > 1$ m s^{-1} and phase speeds that increase by 50%. (b) Together, background velocity and stratification limit the transmission of mode-1 semidiurnal internal tides at different angles of incidence (shaded regions indicate transmission. Waves propagating parallel to the Gulf Stream have a transmission angle of zero. (c) Transmitted waves are significantly refracted. Incident waves that oppose the flow ($\theta > 90°$) can turn almost directly upstream ($\theta \approx 180°$). In Figure 16c, transmission angles are omitted for incident angles that lead to reflection.

7.3.2. Application to Gulf Stream

Equations (20) and (21) are evaluated using the semidiurnal mode-1 phase speed and effective mean flow ($V = \bar{U}_{11}$) from a two-dimensional cross section of the Gulf Stream taken from the realistic simulation. The phase speed and mean flow vary across the Gulf Stream, altering the maximum and minimum angles of incidence for semidiurnal internal-tide transmission [based on (21); Figure 16]. In general, mode-1 internal tides with angles of incidence $\theta < 60°$ or $\theta > 120°$ are reflected at some point within the Gulf Stream. However, incident tides with small angles of incidence are reflected on the shoreward edge of the Gulf Stream, by the following mean flow, while incident tides with large angles of incidence are reflected on the seaward edge of the Gulf Stream, by the change in phase speed (Figure 16b). Mode-1 internal tides that propagate through the entire Gulf Stream without reflection, propagate more obliquely after transmission [based on (20); Figure 16c].

The realistic simulation of the Middle Atlantic Bight region includes a variety of internal-tide sources and a curved Gulf Stream, making it difficult to identify a precise angle of incidence to compare with the simplified theory. However, the altered pattern of mode-1 sea-surface elevations in the presence of the Gulf Stream (Figure 4) and deflection of energy flux (Figure 15) are consistent with the prediction that the Gulf Stream significantly refracts and/or reflects mode-1 internal tides.

8. Summary and Implications

We have derived vertical-mode momentum and energy balances for small-amplitude internal tides in a slowly varying horizontally and vertically variable flow and density fields. The balances accurately describe tide-mean-flow interactions in a realistic data-assimilative primitive-equation simulation of the Middle Atlantic Bight region, which includes both a shelfbreak front and the Gulf Stream. The applicability of our novel internal-tide/background-ocean momentum and energy balances suggests that simple linear internal-tide models may be improved by incorporating horizontally and vertically variable slowly varying density and subtidal flows, which could be obtained from observations or from a

regional/general-circulation model. Further development of this approach and its application is the subject of *Kelly et al.* [2016].

The shelfbreak front both alters topographic internal-tide generation and, with the corresponding shelf stratification, contributes to horizontally variable eigenspeeds. The former effect decreases topographic internal-tide generation by $\mathcal{O}(10\%)$ (additional simulations indicate that very strong fronts, which were not observed during the summer of 2006, may alter generation by about $\pm 20\%$). The latter effect alters internal-tide wavelength and propagation speed on the shelf, producing $\mathcal{O}(4\ h)$ changes in internal-tide arrival time at a location 40 km onshore of the shelfbreak (although, the spatial distribution of these errors depends on the complicated 2-D interference pattern produced as internal tides propagate away from different generation regions along the shelfbreak). These results suggest that internal-tide predictions near the shelfbreak can particularly benefit from the inclusion of horizontally variable stratification and its (sub)-mesoscale variability, even if the accompanying dynamically balanced subtidal flows are neglected.

The Gulf Stream can (i) produce local patches of mode-1 energy-flux divergence that are comparable in magnitude to topographic internal-tide generation at the shelfbreak and (ii) cause mode-1 tides with an angle of incidence $\theta < 60°$ or $\theta > 120°$ to reflect back to the coast, preventing their radiation into the center of the North Atlantic. The former effect is largely due to mode-1 energy advection by the mean flow, which complicates local energy balances but does not produce a net source or sink of internal-tide energy. The latter effect can be explained using geometric wave theory. These results have broad implications for internal-tide predictions and tidally driven mixing in the Middle Atlantic Bight region. First, a significant fraction of internal-tide energy may be trapped between the coast and the Gulf Stream, leaving more tidal energy available for coastal and slope-region mixing. Second, the precise amplitude, phase, and location of internal tides along the coast may depend heavily on the exact state of the Gulf Stream and its accompanying eddies and meanders.

Other future work would include nonhydrostatic dynamics, nonlinear wave-wave interactions, and nonlinear free-surface in the theory and analysis. The use of higher-order numerics for the modal momentum and energy equations would also allow phase-resolved forecasts and analysis of internal-tide interactions at longer-range. More detailed studies of the effects of internal tides on the subtidal features themselves, from (sub)mesoscales to large-scales, are also needed. Finally, even though the present study focuses on the Middle Atlantic Bight region, similar shelfbreak front and larger-scale currents occur elsewhere in the world's oceans. Applying the present approach to such locations is likely to be revealing.

References

Alford, M. H., and Z. Zhao (2007), Global patterns of low-mode internal-wave propagation. Part II: Group velocity, *J. Phys. Oceanogr.*, *37*, 1849–1858, doi:10.1175/JPO3086.1.

Alford, M. H., J. A. MacKinnon, Z. Zhao, R. Pinkel, J. Klymak, and T. Peacock (2007), Internal waves across the Pacific, *Geophys. Res. Lett.*, *34*, L24601, doi:10.1029/2007GL031566.

Bühler, O. (2009), *Waves and Mean Flows*, Cambridge University Press, Cambridge, U. K.

Chapman, D. C., and M. C. Hendershott (1981), Scattering of internal waves obliquely incident upon a step change in bottom relief, *Deep Sea Res., Part A*, *11*, 1323–1338, doi:10.1016/0198-0149(81)90,037-6.

Chapman, N. R., and J. F. Lynch (2010), Editorial: Special issue on the 2006 shallow water experiment, *IEEE J. Oceanic Eng.*, *1*(35), 1–2.

Chavanne, C., P. Pflament, D. Luther, and K. Grugel (2010), The surface expression of semidiurnal internal tides near a strong source at Hawaii. Part II: Interactions with mesoscale currents, *J. Phys. Oceanogr.*, *40*, 1180–1200.

Chen, D., H. W. Ou, and C. Dong (2003), A model study of internal tides in coastal frontal zone, *J. Phys. Oceanogr.*, *33*, 170–187.

Chuang, W., and D. P. Wang (1981), Effects of a density front on the generation and propagation of internal tides, *J. Phys. Oceanogr.*, *11*, 967–996.

Colosi, J. A., R. C. Beardsley, J. F. Lynch, G. Gawarkiewicz, C.-S. Chiu, and A. Scotti (2001), Observations of nonlinear internal waves on the outer New England continental shelf during the summer Shelfbreak Primer study, *J. Geophys. Res.*, *106*, 9587–9601.

Duda, T. F., Y.-T. Lin, A. E. Newhall, K. R. Helfrich, W. G. Zhang, M. Badiey, P. F. J. Lermusiaux, J. A. Colosi, and J. F. Lynch (2014a), The "Integrated Ocean Dynamics and Acoustics" (IODA) hybrid modeling effort, in *Proceedings of the International Conference on Underwater Acoustics-2014 (UA2014)*, edited by J. S. Papadakis, and L. Bjorno, pp. 621–628, 2nd International Conference and Exhibition on Underwater Acoustics, Rhodes, Greece.

Duda, T. F., W. G. Zhang, K. R. Helfrich, A. E. Newhall, Y.-T. Lin, J. F. Lynch, P. F. J. Lermusiaux, P. J. Haley, Jr., and J. Wilkin (2014b), Issues and progress in the prediction of ocean submesoscale features and internal waves, in *St. John's OCEANS'14 MTS/IEEE*, edited by D. O'Neill, IEEE, St. John's, N. L., Canada.

Dunphy, M., and K. G. Lamb (2014), Focusing and vertical mode scattering of the first mode internal tide by mesoscale eddy interaction, *J. Geophys. Res. Oceans*, *119*, 523–536, doi:10.1002/2013JC009293.

Egbert, G. D. (1997), Tidal data inversion: Interpolation and inference, *Prog. Oceanogr.*, *40*, 81–108.

Egbert, G. D., and R. D. Ray (2003), Semi-diurnal and diurnal tidal dissipation from TOPEX/Poseidon altimetry, *Geophys. Res. Lett.*, *30*(17), 1907, doi:10.1029/2003GL017676.

Gangopadhyay, A., A. R. Robinson, P. J. Haley Jr., W. G. Leslie, C. J. Lozano, J. J. Bisagni, and Z. Yu (2003), Feature-oriented regional modeling and simulations in the Gulf of Maine and Georges Bank, *Cont. Shelf Res.*, 23(3), 317–353.

Garrett, C., and E. Kunze (2007), Internal tide generation in the deep ocean, *Annu. Rev. Fluid Mech.*, 39, 57–87, doi:10.1146/annurev.fluid.39.050,905.110,227.

Gawarkiewicz, G., F. Bahr, R. C. Beardsley, and K. H. Brink (2001), Interaction of a slope eddy with the shelfbreak front in the Middle Atlantic Bight, *J. Phys. Oceanogr.*, 31(9), 2783–2796.

Griffiths, S. D., and R. H. J. Grimshaw (2007), Internal tide generation at the continental shelf modeled using a modal decomposition: Two-dimensional results, *J. Phys. Oceanogr.*, 37, 428–451.

Haley, P. J., Jr., and P. F. Lermusiaux (2010), Multiscale two-way embedding schemes for free-surface primitive equations in the "Multidisciplinary Simulation, Estimation and Assimilation System", *Ocean Dyn.*, 60, 1497–1537.

Haley, P. J., Jr., A. Agarwal, and P. F. J. Lermusiaux (2015), Optimizing velocities and transports for complex coastal regions and archipelagos, *Ocean Modell.*, 89, 1–28, doi:10.1016/j.ocemod. 2015.02.005.

Helfrich, K. R., and W. K. Melville (2006), Long nonlinear internal waves, *Annu. Rev. Fluid Mech.*, 38, 395–425.

Hendry, R. M. (1977), Observations of the semidiurnal internal tide in the western North Atlantic Ocean, *Philos. Trans. R. Soc. London*, 286, 1–24.

Holloway, P., E. Pelinovsky, and T. Talipova (2002), Internal tide transformation and oceanic internal solitary waves, in *Environmental Stratified Flows, Topics in Environmental Fluid Mechanics*, vol. 3, edited by R. Grimshaw, pp. 29–60, Springer, N. Y.

Huthnance, J. M. (1995), Circulation, exchange and water masses at the ocean margin: The role of physical processes at the shelf edge, *Prog. Oceanogr.*, 35(4), 353–431.

Ivey, G. N. (2011), Tides and internal waves on the continental shelf, in *Operational Oceanography in the 21st Century*, vol. 1, edited by A. Schiller and G. B. Brassington, pp. 225–235, Springer, Dordrecht.

Kelly, S. M., J. D. Nash, K. I. Martini, M. H. Alford, and E. Kunze (2012), The cascade of tidal energy from low to high modes on a continental slope, *J. Phys. Oceanogr.*, 42, 1217–1232, doi:10.1175/JPO-D-11-0231.1.

Kelly, S. M., N. L. Jones, and J. D. Nash (2013), A coupled model for Laplace's tidal equations in a fluid with one horizontal dimension and variable depth, *J. Phys. Oceanogr.*, 43, 1780–1797, doi:10.1175/JPO-D-12-0147.1.

Kelly, S. M., N. L. Jones, G. I. Ivey, and R. N. Lowe (2015), Internal tide spectroscopy and prediction in the Timor Sea, *J. Phys. Oceanogr.*, 45, 64–83.

Klymak, J. M., M. H. Alford, R.-C. Lien, Y. J. Yang, and T.-Y. Tang (2011), The breaking and scattering of the internal tide on a continental slope, *J. Phys. Oceanogr.*, 41, 926–945, doi:10.1175/2010JPO4500.1.

Klymak, J. M., M. Buijsman, S. Legg, and R. Pinkel (2013), Parameterizing baroclinic internal tide scattering and breaking on supercritical topography: The one- and two-ridge cases, *J. Phys. Oceanogr.*, 43, 1380–1397, doi:10.1175/JPO-D-12-061.1.

Kunze, E. (1985), Near-inertial wave propagation in geostrophic shear, *J. Phys. Oceanogr.*, 15, 544–565.

Kurapov, A. L., J. S. Allen, and G. D. Egbert (2010), Combined effects of wind-driven upwelling and internal tide on the continental shelf, *J. Phys. Oceanogr.*, 40(4), 737–756.

Lamb, K. G. (2004), Nonlinear interaction among internal wave beams generated by tidal flow over supercritical topography, *Geophys. Res. Lett.*, 31, L09313, doi:10.1029/2003GL019393.

Lamb, K. G. (2014), Internal wave breaking and dissipation mechanisms on the continental slope/shelf, *Annu. Rev. Fluid Mech.*, 46, 231–254.

Legg, S., and K. M. H. Huijts (2006), Preliminary simulations of internal waves and mixing generated by finite amplitude tidal flow over isolated topography, *Deep Sea Res., Part II*, 53, 140–156.

Lermusiaux, P. F. J. (1999), Data assimilation via Error Subspace Statistical Estimation, Part II: Mid-Atlantic Bight shelfbreak front simulations, and ESSE validation, *Mon. Weather Rev.*, 127(7), 1408–1432, doi:10.1175/1520-0493(1999)127 < 1408:DAVESS>2.0.CO;2.

Lermusiaux, P. F. J. (2002), On the mapping of multivariate geophysical fields: Sensitivities to size, scales, and dynamics, *J. Atmos. Oceanic Technol.*, 19(10), 1602–1637.

Lermusiaux, P. F. J., P. J. Haley Jr., W. G. Leslie, O. Logoutov, and A. R. Robinson (2006), Autonomous Wide Aperture Cluster for Surveillance (AWACS): Adaptive sampling and search using predictive models with coupled data assimilation and feedback. [Available at http://mseas.mit.edu/archive/AWACS/index_AWACS.html.]

Lermusiaux, P. F. J., X. Jinshan, C.-F. Chen, J. Sen, L. Y. Chiu, and Y.-J. Yang (2010), Coupled ocean–acoustic prediction of transmission loss in a continental shelfbreak region: Predictive skill, uncertainty quantification, and dynamical sensitivities, *IEEE J. Oceanic Eng.*, 35(4), 895–916, doi:10.1109/JOE.2010.2068611.

Lin, Y.-T., A. E. Newhall, T. F. Duda, P. F. J. Lermusiaux, and P. J. Haley, Jr. (2010), Merging multiple-partial-depth data time series using objective empirical orthogonal function fitting, *IEEE J. Oceanic Eng.*, 35(4), 710–721, doi:10.1109/JOE.2010.2052875.

Linder, C. A., and G. Gawarkiewicz (1998), A climatology of the shelfbreak front in the Middle Atlantic Bight, *J. Geophys. Res.*, 103, 18,405–18,423.

Logutov, O. G., and P. F. J. Lermusiaux (2008), Inverse barotropic tidal estimation for regional ocean applications, *Ocean Modell.*, 25, 17–34.

Marshall, J., A. Adcroft, C. Hill, L. Perelman, and C. Heisey (1997), A finite-volume, incompressible Navier-Stokes model for studies of the ocean on parallel computers, *J. Geophys. Res.*, 102, 5753–5766.

Munk, W. H., and D. E. Cartwright (1966), Tidal spectroscopy and prediction, *Philos. Trans. R. Soc. London*, 259, 533–581.

Nash, J. D., E. Kunze, C. M. Lee, and T. B. Sanford (2006), Structure of the baroclinic tide generated at Kaena Ridge, Hawaii, *J. Phys. Oceanogr.*, 36, 1123–1135, doi:10.1175/JPO2883.1.

Nash, J. D., S. M. Kelly, E. L. Shroyer, J. N. Moum, and T. F. Duda (2012), The unpredictable nature of internal tides on continental shelves, *J. Phys. Oceanogr.*, 42, 1981–2000, doi:10.1175/JPO-D-12-028.1.

Newhall, A. E., et al. (2007), Acoustic and oceanographic observations and configuration information for the whoi moorings from the SW06 experiment, *WHOI Tech. Rep. WHOI-2007-04*, Woods Hole Oceanogr. Inst., Woods Hole, Mass.

Park, J., and D. R. Watts (2006), Internal tides in the southwestern Japan/East Sea, *J. Phys. Oceanogr.*, 36, 22–34.

Pereira, A. F., B. M. Castro, L. Calado, and I. C. A. da Silveira (2007), Numerical simulation of M_2 internal tides in the South Brazil Bight and their interaction with the Brazil Current, *J. Geophys. Res.*, 112, C04009, doi:10.1029/2006JC003673.

Rainville, L., and R. Pinkel (2004), Observations of energetic high-wavenumber internal waves in the Kuroshio, *J. Phys. Oceanogr.*, 34, 1495–1505.

Rainville, L., and R. Pinkel (2006), Propagation of low-mode internal waves through the ocean, *J. Phys. Oceanogr.*, 36, 1220–1236.

Sharples, J., C. M. Moore, A. E. Hickman, P. M. Holligan, J. F. Tweddle, M. R. Palmer, and J. H. Simpson (2009), Internal tide mixing as a control on continental margin ecosystems, *Geophys. Res. Lett.*, 36, L23603, doi:10.1029/2009GL040683.

St. Laurent, L., and C. Garrett (2002), The role of internal tides in mixing the deep ocean, *J. Phys. Oceanogr.*, 32, 2882–2899.

Tang, D., et al. (2007), Shallow Water 06: A joint acoustic propagation/nonlinear internal wave physics experiment, *Oceanography*, 20, 156–167.

Tennekes, H., and J. L. Lumley (1972), *An First Course in Turbulence*, MIT Press, Cambridge, Mass.

Ueckermann, M. P., and P. F. J. Lermusiaux (2010), High order schemes for 2D unsteady biogeochemical ocean models, *Ocean Dyn.*, 60(6), 1415–1445, doi:10.1007/s10236-010-0351-x.

Ueckermann, M. P., and P. F. J. Lermusiaux (2016), Hybridizable discontinuous Galerkin projection methods for Navier–Stokes and Boussi-nesq equations, *J. Comput. Phys.*, *306*, 390–421.

Venayagamoorthy, S. K., and O. B. Fringer (2006), Numerical simulations of the interaction of internal waves with a shelf break, *Phys. Fluids*, *18*(7), 076603.

Zaron, E. D., and G. D. Egbert (2014), Time-variable refraction of the internal tide at the Hawaiian Ridge, *J. Phys. Oceanogr.*, *44*, 538–557.

Zhang, Y. G., and T. F. Duda (2013), Intrinsic nonlinearity and spectral structure of internal tides at an idealized Mid-Atlantic Bight shelf break, *J. Phys. Oceanogr.*, *43*, 2641–2660.